

Cotton Valley Imaging Project
Phase IV
Completion of Microseismic Mapping
of the
Phase I and II Hydraulic Fractures
Wells CGU21-10 and CGU21-09

Report
for
Gas Research Institute
November, 1999

James Rutledge[◇] and Ted Urbancic*

◇ Los Alamos National Laboratory, GeoEngineering Group / EES-4, Mail Stop D443, Los Alamos, NM 87545
505-667-8938, jrutledge@lanl.gov

* Engineering Seismology Group Canada, Inc., 1 Hyperion Court, Kingston, Ontario, Canada, K7K 7G3
613-548-8287, urbancic@esg.ca

Introduction

Microseismic monitoring was conducted for three stages of hydraulic fracture completions of wells CGU21-10 (Phase 1) and CGU21-09 (Phase 2) in May and July, 1997, respectively. ARCO wrote two reports summarizing the acquisition and field analysis of the Phase-1 and -2 microseismic data (Withers and Dart, 1997a; Withers and Dart, 1997b). The Phase 1 preliminary mapping results of ARCO were also presented in Walker (1997).

ARCO mapped subsets of the data collected in the field using their process of visually matching calculated wavefront curves with full-array waveform displays. Based on an operator moving a graphical display of a trial event location, a single event's final location is stored when the operator finds an acceptable match of the corresponding display of computed and observed arrival times. Los Alamos, The Engineering Seismology Group Canada (ESG), and Sandia each separately mapped different subsets of the Phase-1 data and presented preliminary results at the December, 1997 meeting of the Cotton Valley Imaging Consortia. The ESG analysis also include characterization of the microearthquake source parameters (Urbancic and Zinno, 1998). At the same meeting, ARCO presented their mapping results of the Phase-2 data. A number of problems or discrepancy were identified that warranted a more thorough investigation of the data and the various mapping techniques employed. After two preliminary studies investigating the asymmetry of fracture growth of the Phase-1, Stage-2 treatment (Rutledge, 1998) and a re-evaluation of the single-well locations of the Phase-2 data (Urbancic, 1998), the Cotton Valley Consortia, under GRI management, funded both Los Alamos and ESG to complete the microseismic mapping and analysis of source parameters for the entire Phase-1 and -2 data sets.

These efforts constitute Phase IV of the Cotton Valley Imaging Project and include the following tasks:

1. Calculation of event locations using inversion techniques for the Phase 1 and 2 hydraulic fractures (over and above previously located events).
2. Determination of source parameters for the above located events.
3. Confirmation of results through joint analysis of data subsets.
4. Evaluation of velocity and array geometry effects on event location and source parameter determinations.
5. Visualization of results and associated location errors.

Part I of this report covers the microearthquake location analysis and involves tasks 1, 3, 4, and 5; Part II covers the analysis of source parameters and involves tasks 2, 3, 4 and 5.

Data

The treatment and monitor well locations are shown in Figure 1. Details of the geology, fracture design, instrumentation, deployment and data acquisition are described in Walker (1997). Two 2350-ft-long, 48-level, 3-component geophone arrays were permanently installed by attaching the array strings to 2-7/8 inch production tubing and cementing the two strings into wells CGU22-09 and CGU21-09 (Figure 1). Sonde spacing was 50 ft. Signals were amplified 60 dB downhole; an additional 48 dB of gain was applied uphole before digitizing at a 1 msec sample interval.

The geophone array and tubing string in 21-09 were deployed in open hole and jammed during installation. As a result the lower portion of the array was damaged and the well was completed to a depth of only 9108 ft, or about 700 ft shallower than the planned total depth of about 9800 ft. The deepest working geophone station in 21-09 sits above all three completion stages (station 1-34, Figures 2, 3 and 4). The array in 22-09 had functioning receivers over its entire length and spanned all completion stages. Fully-functional 3-component pods in 22-09 spanned all but the Phase-1, Stage-1 (Taylor Sand) treatment. Monitoring of the 21-10 treatments (Phase 1) included the use of both monitor wells; the 21-09 treatments (Phase 2) was monitored using only the 22-09 receiver array. From here on, we refer to the 21-09 array as array-1, and the 22-09 array as array-2. Figures 2, 3 and 4 show the receiver stations used for determining the Phase-1 locations.

Waveform data were translated to local formats. P and S arrival times were picked by visual inspection and stored in the waveform file headers. ESG initially implemented automated pickers and then checked and supplemented the pick data via visual inspection.

Location Technique, Use of Data, and Error Estimation

We use a variation of the Geiger method of earthquake source location determination, by which an inversion scheme is iteratively applied to move the source to a solution (origin time, X, Y, Z)

that minimizes the difference in computed and observed arrival times in a least-squares sense (Aki and Richards, 1980, p. 692). The raytracer used for computing arrival times finds the minimum time paths through a flat-layered velocity structure and is able to account for critically refracted travel paths and low-velocity layers. The Geiger method has been generalized to include directional particle-motion data (hodograms), so that misfit of both traveltime and angular data are minimized. This modified Geiger approach forms the kernel of a Joint Hypocenter Determination (JHD) inversion scheme that simultaneously solves for origin time, X, Y, Z and the station corrections for a population of microearthquakes by minimizing

$$\sum_{ij} R_{ij}^2 = \sum_{ij} \left[\left(\frac{tp_{ij}^o - tp_{ij}^p}{w_i^p} \right)^2 + \left(\frac{ts_{ij}^o - ts_{ij}^p}{w_i^s} \right)^2 + \left(\frac{\theta_{ij}^o - \theta_{ij}^p}{w_i^\theta} \right)^2 \right] \quad (1)$$

where tp_{ij}^o is the observed P arrival time at station i for event j , tp_{ij}^p is the predicted P time for the same station-event pair given the estimated microearthquake location and origin time, and ts_{ij}^o and ts_{ij}^p are the corresponding times for S waves. θ_{ij}^o and θ_{ij}^p are the observed azimuth (from the hodogram data) and the azimuthal position of the estimated microearthquake location, respectively, for event j with respect to station i . Weighting of the arrival-time and hodogram data is done by setting w_i^p , w_i^s and w_i^θ equal to the estimated random data errors at station i . The random data errors are estimated in initial test location runs as the standard deviation of the corresponding residual terms (observed minus predicted values). Alternatively, the hodogram data errors can be estimated beforehand from the scatter of data between adjacent sondes (described below).

In general, using the statistics of misfit for a population of events, the JHD approach allows the determination and removal of systematic errors (station corrections) due to systematic picking errors or velocity model variations. The JHD approach results in a more precise relative location of sources, that is, it improves the overall image and estimation of fracture height and length delineated by the induced events. The best absolute position of the population of microearthquakes depends on how well the seismic velocities are known. Velocity calibration is discussed below.

Hodogram Data

The hodogram data are derived from the horizontal components' first motion data to provide an azimuth from receiver to source. When mapping event locations from a single well, the travel time data only constrain the depth and radial source position from the line array; the hodogram data are required to independently determine the azimuthal position from the well. Hodogram data are not as critical for multiple-well data, but are still very useful for resolving ambiguities from 2-well locations (see Figure 3 of Rutledge, (1998)) and for providing additional data constraints when determining seismic velocities. We have computed azimuths as the principle eigenvector fitting the first 6 msec of P-wave data (Flinn, 1965). (Eigenvector analysis can essentially be thought of as fitting an ellipse to the particle motion data.) S-wave first motion data also provided high quality azimuthal data, and is discussed further below in the presentation

of the Phase 2 results. Orientations of the geophones' horizontal components were determined from multiple, high-quality calibration shots fired in well 21-10.

Selection criteria for the use of hodogram data was based on: 1) the consistency of data obtained from multiple sondes; 2) first arrival signal-to-noise ratios (S/N); and 3) the linearity of particle motion. For a given source, the azimuths obtained from different sondes in a vertical array should, in principal, differ by a constant representing the difference in sonde orientation. A scatter plot of relative azimuths obtained from two sondes of the Phase-1, Stage-2 data is shown in Figure 5. As would be expected, the scatter increases as S/N degrades. Selection criteria for use of the hodogram data is represented by the shaded area (i.e., $S/N \geq 5$ and $\Delta\text{azimuth} \leq \pm 6^\circ$ from the median difference). In addition, a linearity constraint of $\lambda_1 / (\lambda_1 + \lambda_2) \geq 0.95$ was imposed, where λ_1 and λ_2 are the major and minor axes of the ellipse fitting the data (the square-roots of the eigenvalues), respectively. A value of 1.0 would be perfectly linear. Random hodogram data error was estimated as the standard deviation of the relative azimuths about the mean difference. Within the selection criteria used, angular error ranged from about $\pm 2.5^\circ$ to $\pm 3^\circ$.

The mean or median $\Delta\text{azimuth}$, as seen in Figure 5, provides a fairly robust measurement of relative sonde orientations. If at least one sonde can be accurately oriented absolutely, using calibration shots or by other means, then all other sonde orientations can be accurately determined using the high quality microearthquake data.

Velocity Calibration

Ample velocity data are available from the Cotton Valley study area to help constrain the velocity models used to locate the microearthquakes. These include P and S sonic logs and a set of primacord shots fired in well 21-10 and recorded on both arrays. A perforation-gun subassembly was used to detonate the primacord and was equipped with a geophone in the cablehead to provide detonation time. Finding a universal model that best fits all the data simultaneously is difficult without compromising the misfit associated with the event locations of individual treatments. Each data set can be optimally mapped using different sets of receivers, depending on the depth interval of the treatment and what receivers were operating. Since different combinations of layers are sampled by the various data sets, our approach is to calibrate the velocities independently for each treatment using the available velocity data and the microearthquake data itself. Further, hydraulic fracture microseismicity allows an ad hoc approach to calibrating the seismic velocities, knowing that the linear trends of seismicity should align with the treatment well.

Figure 6 is a preliminary location map of the Phase-1, Stage-3 data based on a 6-layer model derived from the sonic logs (Figure 7). These are the highest quality event locations from the stage 3 treatment based on the individual-event residual terms (Equation 1) and the data available (multiple hodogram and P- and S-travel-time data from both arrays). Use of the sonic log velocities, in general, results in the microearthquake locations of all the data sets to align too far north of the treatment well (21-10 in Figure 6). The linear trends and depth distribution of events changes little for velocities varying within a reasonable range. But best position of the trend cannot be resolved with the JHD in terms of Equation 1 because velocity changes are simply traded off for station correction changes. Our ad hoc approach for calibrating velocity is to find

the best fit model that results in the microearthquakes aligning with the treatment well. Based on the initial JHD results, using the sonic log model (Figure 7), we measure the linear trend of the highest quality locations (e.g. Figure 6) and shift the X, Y locations so that the line intersects the treatment well. Z was already constrained and fairly insensitive to velocity due to the receivers spanning the treatment interval, and so was kept fixed. Particle motion data was honored in the shift, by adding a rotational correction equal to the mean azimuthal residual for 2-well data ($< 2^\circ$), or, for single-well data, by shifting along an event's mean hodogram azimuth. Keeping the new (shifted) X, Y, Z locations fixed, we then invert to solve for the best fit velocity model and new origin times, again, in the sense of minimizing Equation 1. The shot data, with their X, Y, Z and origin times known, can also be included as input data for further constraining the velocity inversion.

With the new velocity model, we then re-run all the events through the JHD to solve for new X, Y, Z, origin time and station correction values as described above. As would be expected, the final station corrections are small (weighted averages < 1 msec). The model results are not unique, but simply provide a reasonable velocity structure that aligns the known seismicity trends as we expect it, intersecting the treatment well. The final locations for the Phase-1, Stage-3 data are shown in Figure 12. Figure 7 shows both the starting and final models of the Stage-3 velocity inversion.

Mapping Results

Phase 1, Stage 1 (CGU21-10, Taylor Sand)

These data were some of the most difficult to map due to location of most working receivers hundreds of feet above the treatment zone and low S/N data. About 110 events were recorded. ARCO mapped all the events in the field. Their locations extended about 1100 ft east of the treatment well, terminating near the plane of the two monitor wells. A mirror location ambiguity exists along the plane of the two monitor wells and can best be resolved by using hodogram data, if available (see Figure 3 in Rutledge, (1998)). ARCO did not use hodogram data (Withers and Dart, 1997a). Sandia mapped the microearthquakes using the single-well data from array-2, requiring them to use hodograms to constrain azimuths (Warpinski, et al., 1997). Sandia's locations indicated the fracture extended approximately 1800 ft east of the treatment well, that is, about 700 ft longer than ARCO's estimate. Our locations confirm the Sandia estimation of eastward fracture growth.

Seventy five events were located (Figure 8). All the mapped events had multiple P- and S-arrivals identified on array-2, and 67 of the mapped events had at least one S-arrival on the deepest working receiver of array-1 (station 1-34). Due to the poor S/N of the P-arrivals, we used the S-wave particle motions to determine azimuths and relaxed the constraint of Δ azimuth between sondes from $\leq \pm 6^\circ$ to $\leq \pm 15^\circ$. Fifty seven of the 75 located events had azimuthal data within this constraint, with an estimated error of $\pm 6.5^\circ$ (standard deviation). For most events having at least one arrival from array-1 allowed us to unweight the hodogram data relative to the traveltimes data. Most importantly, the hodogram data allowed us to start the locations on the correct side of the plane of the two monitor wells.

Projections of the error ellipsoids are shown in Figure 9. The median principal error axes is ± 33

ft. As in all location errors presented in this report, the errors only reflect the distributions of data types, the station-event geometry and the data uncertainties. The velocity model is considered to be correct.

Phase 1, Stage 2 (CGU21-10)

The locations of the Stage-2 microearthquakes are presented in Rutledge (1998). A total of 1167 triggered events were recorded. As discussed in that report, about 100 low-magnitude events occurred near the eastern terminus of seismicity that had large errors because of their proximity to the plane of the two monitor wells and a lack of reliable P-wave hodogram data to constrain their lateral positions. This subset of events was remapped using the higher amplitude S-wave data for azimuthal data, which clearly indicate that the fracture only extends eastward about 1000 ft (Figure 10). Velocities were also re-calibrated in the manner described above. A total of 924 events were located.

Only a handful of events indicate activity outside the perforated interval. Stress profiling in the Upper Cotton Valley indicate that the stress gradients alone are too low to confine height growth; stratigraphy may be a factor in controlling height growth (Pinnacle Technologies, 1999). The lateral extent of seismicity for the Stage 2 treatment is symmetric about the treatment well. However, the growth patterns, source characteristics and energy distribution of seismicity are highly asymmetric (Urbancic, et al., 1999). There is a gap in seismicity about 400 ft west, followed further westward by an offset northward and continuation of the trend (Figure 10). Interestingly, the westward extent of the Phase 1, Stages-1 and -3 seismicity are both about 400 ft (Figures 8 and 12, stage 3 has only two events west of 400 ft). A structural discontinuity at about 400 west, such as a steep crosscutting fault, may be impeding or altering fracture growth further westward.

Projections of the error ellipsoids are shown in Figure 11. To reduce overprinting, every 5th error ellipsoid is plotted after sorting events west to east. The median principal error axes is ± 21 ft.

Phase 1, Stage 3 (CGU21-10)

ARCO recorded 1122 triggers during this treatment. Picks were made on 760 events, of which 696 were located (Figure 12). Representative error ellipsoids are displayed in Figure 13. The median principal error axes is ± 25 ft. Most of the seismicity occurs within the perforated interval and defines two distinct depth intervals of seismicity. High-precision, relative mapping of the Stage-2 data indicates that most of the detected seismicity during that treatment was actually confined to a 10 ft depth interval, or about 4% of the total injection depth interval (Rutledge, et al., 1998). These patterns indicate that the detectable seismicity is restricted to certain lithologic units, perhaps controlled by a Hill-type mesh of affected fractures in alternating competent and incompetent strata (Hill, 1977; Sibson, 1996). The induced seismicity indicates some downward growth of the Stage 3 treatment; upward growth is contained (Figure 12). Downward growth terminates at the upper boundary of the Stage-2 treatment (Figures 12 and 10).

Phase 2 Data (CGU21-09)

Microseismic monitoring of the CGU21-09 treatments (Phase 2) was done using the stations still operating in 22-09 (array-2) (Withers and Dart, 1997b). Since these are single-well data,

hodogram data are required to determine source azimuths from the receiver array. In general, P-wave arrivals for the Phase-2 data had lower S/N than the Phase-1 data. ARCO located small subsets of the Phase-2 microearthquakes. Their maps showed unreasonable arcing features with the 22-09 monitor well at the center, indicating a problem with the hodogram data or with their implementation of determining azimuths from the P-wave particle motion data (Figure 14). ESG independently located the same event subsets using azimuthal data derived from eigenvalue/eigenvector analysis of both P- and S-wave particle motion data, The ESG results showed linear trends of seismicity along the anticipated fracture orientation (Urbancic, 1998). As noted in Urbancic’s report, since the S-waves characteristically exhibit stronger arrivals, using the S-wave based hodograms promises greater reliability for single-well mapping of hydraulic fractures. A closer look at the S-wave hodogram data shows this indeed to be true.

The most limiting data factor in single-well mapping is the quality of hodogram data. Highly reliable travelttime data can be obtained from marginal S/N arrivals that yield unreliable particle-motion data. Even for good particle motion data (e.g. Figure 5), hodogram errors account for the largest component of location error when considering single-well receiver geometries at Cotton Valley. In a homogeneous medium, the S-wave particle motions should be perpendicular to the P-wave motion. Ideally, a 90° rotation of S-wave hodogram data should yield the same azimuth as P-wave data. A comparison of the S and P horizontal-component particle motions for the higher quality data of Phase-1, Stage-2 show good agreement. Mean differences are about $\pm 2^\circ$ with standard deviations of about 4.5° (Table 1).

| Station | Mean P and S Δ azimuth | Δ azimuth Standard Deviation | number of observations |
|----------------|-------------------------------|-------------------------------------|------------------------|
| 2-38 | 1.9° | 4.0° | 194 |
| 2-30 | -2.2° | 4.7° | 101 |
| 2-24 | 1.8° | 4.5° | 98 |
| All 3 stations | 0.8° | 4.7° | 393 |

Table 1. Comparison of P- and S-wave hodograms for the Phase-1, Stage-2 events in which the P-wave hodograms of all three stations passed the selection criteria, ($S/N \geq 5$, Δ azimuth $\leq \pm 6^\circ$, and linearity $\lambda_1/(\lambda_1 + \lambda_2) \geq 0.95$). Linearity of S-wave particle motions also exceeded 0.95.

In terms of self-consistency, the S-wave-based hodograms show less scatter (smaller errors) and greater percentages of events that pass the selection criteria as outlined above (Figure 15). Hence, the S-wave hodogram azimuths are superior to the P-waves hodograms. For the Phase 2 treatments we used only S-wave hodograms, and at least 2 stations had to meet the selection criteria. Up to six stations were used for hodograms (Figure 16) and most events had 5 or more hodograms meeting the selection criteria. Random angular error was estimated at $\pm 2.5^\circ$, measured as the standard deviation of the Δ azimuths about the mean difference (e.g. Figure 15).

The resultant standard errors of location associated with n angular data are reduced by $1/\sqrt{n}$, so

for a typical Phase-2 event, constrained by 5 or 6 hodograms, random angular error is reduced to about $\pm 1^\circ$. At 1500 ft distance from the monitor well, this corresponds to about ± 25 ft, comparable to errors associated with the random traveltimes errors. Systematic angular error cannot be determined from the single-well data, however, the mean angular residuals of the two-well, Phase-1 data were on average less than 1° .

Thirteen stations spanning nearly 2000 ft were considered for P and S traveltimes data (Figure 16). S-arrivals could often be observed over the whole array length; P-waves could rarely be observed above station 2-21. In consideration of the S-wave hodogram data and the vertical distribution of P- and S-wave data, the Phase 2 data are of high quality for determining locations. The angular position of the monitor well with respect to the treatment well and anticipated fracture orientation is also ideal for detecting fracture wing asymmetry. That is, range of detection for both wings is equal.

Because the CGU21-09 well was completed shallower than planned, the treatment intervals differ from the more typical Phase-1 intervals. The 3 completion stages for CGU21-09 (Phase 2) correspond to sub-intervals of the Stage 3 and the upper-most section of Stage 2 of the Phase 1 stimulations (compare Figure 16 with Figures 2, 3 and 4).

Phase 2, Stage 1 (CGU21-09)

Of 554 events detected, 437 have been located (Figure 17). Height growth is contained. Seismic gaps, 300 to 400 ft long, separate three groups of induced seismicity. The most populous group, by far, is the eastern most cluster extending about 1300 ft from the treatment well. Seismicity only extends about 600 ft west. There also appears to be an offset or a change in linear trend associated with the eastern-most cluster.

Representative error ellipsoids are shown in Figure 18. The median principle error axes is ± 25 ft.

Phase 2, Stage 2 (CGU21-09)

Of 310 events detected, 118 were located (Figure 19). Seismicity is fairly evenly distributed along the linear trend. The west wing is longer than the east (about 750 and 550 ft respectively). Most events occur within the perforated interval, but there is evidence of height growth, predominantly downward to a zone lying just above the previously treated Stage 1 interval. This treatment depth interval corresponds to the base of the Phase-1, Stage-3 treatment, which exhibited very similar downward growth (compare with Figure 12).

Error ellipsoids are shown in Figure 20. The median principle error axes is ± 23 ft.

Phase 2, Stage 3 (CGU21-09)

Of 975 triggered events, 225 were located (Figure 21). Like the Stage 2 treatment, growth extends further westward (about 800 ft west and 600 ft east). Height growth is contained. There is a gap in seismicity from about 100 to 300 ft west of the well. Like the offset and terminations of seismicity at 400 ft west of the 21-10 treatments (Phase 1), it is interesting that the eastern wings of Phase 2, Stages-2 and -3, the shorter wing for both, terminate at about +1700 ft east, the same location at which there appears to be an offset and the start of the anomalous, eastern-most

cluster of Stage 1 (Figures 17, 19 and 21). Perhaps, again, this could be related to some structural discontinuity there that impedes or alters growth eastward, such as a steep crosscutting fault.

Error ellipsoids are shown in Figure 22. The median principle error axes is ± 24 ft.

Summary: Microseismic Locations

The fracture orientations and wing lengths of all six treatment are summarized in Table 2. Wing lengths are reported as the extreme locations. Orientations were computed by linear regression of the microearthquake X, Y locations. All six hydraulic fracture trends are oriented at N78°E.

| Well (Phase) | Treatment | Orientation | Wing Lengths (ft) | |
|------------------|--------------------|------------------|-------------------|------|
| | | | West | East |
| 21-10 Phase 1 | Stage 1 (05/12/97) | 77.6° \pm 0.9° | 400 | 1800 |
| | Stage 2 (05/14/97) | 78.3° \pm 0.3° | 950 | 1000 |
| | Stage 3 (05/16/97) | 78.2° \pm 0.3° | 750 | 1300 |
| 21-09 Phase 2 | Stage 1 (07/14/97) | 77.6° \pm 0.3° | 600 | 1300 |
| | Stage 2 (07/16/97) | 78.2° \pm 0.7° | 750 | 550 |
| | Stage 3 (07/18/97) | 78.6° \pm 0.6° | 800 | 600 |

Table 2. Summary of treatment wing lengths and fracture orientations. Orientations were computed by linear regression of the microearthquake X, Y locations. Orientation of the Phase-1, Stage-2 treatment only used locations east of -400 ft (Figure 10).

Interpretation of fracture asymmetry for the Phase-1 treatments is ambiguous because of the detection range differences between the west and east wings (e.g. Rutledge, 1998). That ambiguity does not exist for the Phase-2 data, and the seismicity of each treatment exhibits asymmetry with the preferential direction of growth varying between the sequential treatment depth intervals. The Phase-1, Stage-2 microseismicity exhibits the most symmetric distribution of all (Figure 10), yet the temporal growth patterns, source characteristics and energy distribution of seismicity are highly asymmetric (Urbancic, et al., 1999). Offsets and/or trend changes in the seismicity, such as at 400 ft west of Phase 1, Stage 2 (Figure 10) and at 600 ft east of Phase 2, Stage 1 (Figure 17) correlate with termination of seismicity in the other respective treatments of Phases 1 and 2, perhaps suggesting crosscutting structures that alter or impede fracture wing growth. Analysis of the source parameters and the temporal patterns of location and source characteristics, correlated with the treatment histories can provide much more information on the dynamics and heterogeneities associated with fracture growth. Part 2 of the Phase IV analysis covers some of these aspects of the microseismic data.

Part II: Source Parameters

Introduction

The recording of full triaxial waveforms provides an opportunity to obtain additional characteristics (parameters) of the seismic source, such as strength, slip dimensions, seismic energy and stress release, and further used to delineate modes of failure, identify changing stress conditions within a seismogenic volume, and subsequently insight into the conditions under which failures perpetuate (e.g., Urbancic and Trifu, 1997). Based on many reported observations, we can suggest that spatial / temporal variations in microseismic source parameters provide a means to assess the effectiveness of hydraulic fractures for stimulating reservoir production and potentially to validate / calibrate fracture model designs (i.e., fracture staging, fluid and proppant volumes).

The feasibility of determining / employing source parameters for the characterization of hydraulic fracture behaviour in the Cotton Valley was carried out by Urbancic and Zinno (1998). In their study, source parameters were calculated for events with high signal-to-noise ratios (79) recorded during the May 14, 1997 Stage 2 fracture treatment. They showed that little energy was imparted during the fracture process as evidenced by the relatively small event magnitudes (-1.5 to 0) and stress drops obtained. The S- to P-wave energy ratios were found to increase with time and distance from the treatment well, suggesting that events close to the treatment well included non-shear components of failure in addition to shearing whereas at the extremities of the hydraulic fracture the fracturing processes was dominated by shear failures. Further analysis of the Stage 2 data set by Urbancic et al. (1999; see attached), as outlined by the spatial / temporal / frequency variations in magnitude, suggested that fracture growth tended to be rapid following injections and that the fracture behaved characteristically different with position relative to the treatment well. Based on Frequency-Magnitude Distribution (FMD) parameters (seismic activity level and b-value), east of the treatment well failures were considered to have occurred along multiple orientations under low effective stress levels whereas to the west of the treatment well, the FMD parameters suggest that failures were along a predominant or single orientation under higher effective stress. These observations suggest that fracture development is highly dependent on the timing and proppant materials used in the injections.

In this section, the calculated source parameters for the events located in Part I, for all stages of hydraulic fracture completions of Phase 1 and Phase 2, are presented and discussed. In particular, variations in magnitude, S- to P-wave energy release, and apparent stress are used to outline the differences in hydraulic fracture behaviour between the different stages.

Source Parameters: Calculations

In this study, source parameters were calculated using waveform characteristics from rotated band-limited P- and S-wave (S_v and S_h) components for individual triaxial

waveforms and their combined values for each event. The approach, as outlined by Urbancic et al. (1996), is based on velocity and displacement waveform characteristics

$$\Omega = \sqrt{4 S_{D2}^{3/2} S_{V2}^{-1/2}}$$

$$f_c = \frac{1}{2\pi} \sqrt{S_{V2} / S_{D2}}$$

$$J = S_{V2}$$

(P- and S-wave peak amplitudes, source signal durations, rise times, and signal fall-off to correct for attenuation effects) obtained automatically in the time domain and used in the calculation of equivalent spectral estimates of the low frequency level (source

$$S_{D2} = 2 \int_0^{\infty} D^2(t) dt$$

$$S_{V2} = 2 \int_0^{\infty} V^2(t) dt$$

strength parameter), corner frequency (dominant source frequency related to source dimensions), and energy flux (used to obtain the radiated seismic energy of either the P- or S-waves). These input allow for the determination of source strength (seismic moment, moment magnitude), seismic energy release, source radius (Madariaga

$$M_o = \frac{4\pi\rho c^3 R \Omega_o}{F_c}$$

source model; Madariaga, 1976), and stress release (static stress drop and apparent

$$E_o = 4\pi\rho c R^2 J$$

$$\Delta\sigma = \frac{7 M_o}{16r_o^3}$$

stress). It is these parameters that are investigated further in this study.

In the time-domain, the three principal parameters, namely the low frequency spectral level (Ω_o), corner frequency (f_c), and energy flux (J), are calculated as (Brune, 1970; Andrews, 1986; Snoke, 1987), where S_{D2} and S_{V2} are integrals of the squared spectral displacement and velocity for both the P- and S-wave trains. By applying Parseval's theorem, these integrals can be converted to the following time integrals where $D^2(t)$ and $V^2(t)$ are calculated by summing the squared double and single integrated P- and S-wave train acceleration components.

Here, we compute the seismic moment (M_o), seismic energy (E_o) and static ($\Delta\sigma$) and apparent (σ_a) stress drop as

$$M = \frac{2}{3} \log(M_o) - 6.0$$

where ρ is the density at the source, c is the wave velocity, R is the source-sensor separation, F_c is the double couple radiation coefficient (0.52 and 0.63 for P- and S-wave; Boore and Boatwright, 1984), μ is the modulus of rigidity, and $r_o = K\beta/2\pi f_c$ is the source radius (K is 2.01 and 1.32 for P- and S-wave; Madariaga, 1976). Additionally, the seismic moment can be used to calculate the moment magnitude

In this analysis, recorded signals were multiplied, to a first approximation, with a constant term $\exp(\pi R f_c / c Q)$ to correct for attenuation. The use of f_c as an average frequency in the on-line approach corresponds to the assumption that signal amplitudes propagating with the corner frequency are much larger than the signal amplitudes at all other frequencies. Q-values were estimated from the decay of the S-wave coda trains as a function of time (coda-Q technique; Sato, 1984) for each component of every triaxial. The coda-Q calculations were based on windows beginning immediately after the maximum S-wave amplitude and extending until the signal to noise ratio fell below 2.0. For most signals analyzed, the Q-values between components were similar (it was assumed that the P- and S-wave Q-values were similar). Assuming that the maximum to minimum Q-value ratio did not exceed 2.5 (an empirically derived limit), the final Q-value applied to a triaxial was an average of the three individual values. In the case where this ratio was exceeded, the ratios of the maximum to intermediate and intermediate to minimum Q-values were determined and the components with the lowest ratio were kept for source parameter calculation. If all ratios were above 2.5, then the triaxial was dropped from the analysis.

Source Parameters: Results

Phase1: Stage 1, 2 and 3 (0512, 0514, and 0516) Treatments

As shown in Figures 23 to 29, the spatial variations in moment magnitude, S-wave to P-wave seismic energy are presented for all three stimulations in the 21-10 treatment well. Additionally, for the 0514 fracture, the apparent stress is also provided. To allow for comparison between treatments, the scaling between figures is consistent.

$$\sigma_a = \frac{\mu E_o}{M_o}$$

Along with contoured views of the source parameters, individual values are also shown so that the range of values can be further assessed.

In Figures 23 to 25, the magnitudes for individual events recorded during the three treatments ranged from about -2 to -1 (Note: for the 0514 treatment, individual values ranged up to -0.5, however for scaling purposes those few events have been omitted from the figure), with the larger events tending to occur on average to the west of the treatment well (most clearly observed for the 0514 fracture). The lack of very small magnitude events to the west of the treatment well are related to array geometry

detectability issues (as we progressively move away from the the monitoring wells, the signals of the smaller events tend to become indistinguishable from the background noise; Rutledge, 1998). The general lack of larger magnitude occurrences to the east of the treatment well, however, can not be explained by array effects and therefore must be considered to represent inherent differences in fracture development on either side of the treatment well.

The above assessment on fracture development is further supported when we consider the ratio of S- to P-wave seismic energy release for the three stimulations in Figures 26 to 28. In all three treatments, the E_s/E_p values tended to vary with position relative to the treatment well. Towards the east, smaller E_s/E_p values (<10) were observed close to the treatment well than at the eastern extremity of the fracture ($E_s/E_p > 10$). If we consider that a decrease in E_s/E_p values is related to the presence of non-shear or volumetric components of failure, than the low E_s/E_p zones may represent the volumetric behaviour of the propped zone and regions of larger E_s/E_p values are likely related to shear-type failures which extend the overall fracture but do not necessarily contribute to the fracture volume. In the 0514 fracture, the mode of failure to the west of the treatment well behaves like a shear failure and therefore, under the above argument, only contributes to the overall fracture length and not necessarily to the propped dimension. In Figure 29, the apparent stress is shown for the 0514 fracture. The high values to the west of the treatment well suggests that the fracture propagated under higher effective stress levels into this region whereas to the east of the treatment well, the fracture propagated under lower effective stress levels, likely related to the presence of fluids. Similar observations in apparent stress drop (and static stress drop) to the east of the treatment well were observed for both the 0512 and 0516 stimulations. Interestingly, the increase in event magnitude observed for the 0516 fracture just to the west of the treatment well is not followed by an increase in E_s/E_p values as seen for 0514, suggesting that the propped zone for 0516 may indeed extend slightly to the west of well 21-10.

Phase 2: Stage 1, 2, and 3 (0714, 0716, and 0718) Treatments

Similar to the Phase 1 analysis, we examined spatial variations in moment magnitude, the ratio of E_s/E_p seismic energies, and apparent stress for all three treatments. Generally, the event magnitudes for these treatments (Figures 30 to 32) were smaller than those observed during Phase 1, particularly when compared to the 0514 and 0516 stimulations. This can likely be attributed to differences in the injection materials used between the two phases, which could further have impacted the proppant volume created versus fracture dimensions.

If we consider the 0714 treatment, the largest event magnitudes occurred to the far east of the treatment well. Interestingly, the E_s/E_p and apparent stress values were also larger for this region, suggesting that most of the failures could be considered as being shear type that have occurred under higher effective stress levels (Figures 33 and 34). As for the other regions of increased event concentration for the 0714 treatment, the E_s/E_p values tend to be higher, however, the apparent stress values are small relative to the far east cluster. This implies that failures close to the treatment well were also shear but that the effective stress levels were small, again likely due to the

presence of fluids. Overall, the 0714 fracture does not appear to have resulted in a well-defined propped zone as outlined by the source parameters in the Phase 1 treatments.

In contrast, the 0716 treatment generally exhibited low E_s/E_p values throughout the fracture volume (figure 35). Following the established line of reasoning above, the failures included a non-shear volumetric component, which, along with the generally lower magnitudes observed, suggest that a larger propped volume was created by the injections than for the 0714 treatment.

The 0718 treatment, again exhibited a different character from that observed for the previous stimulations. In this case, an increase in E_s/E_p occurred just to the west of the treatment well (Figure 36). The corresponding apparent stress values also increased slightly but not to the levels observed for the 0714 treatment (Figure 37). Accordingly, we can suggest that the 0718 treatment resulted in failures dominated by shear type failures with a poorly defined propped zone.

Source Parameters: Summary

In this section, we have examined the waveforms of the located microseismic events for characteristics that allow for the determination of parameters that can more fully describe the source of individual events and the volume within which these events occur. In particular, estimates of strength, energy and stress release were obtained and compared in a spatial / temporal context for the individual treatments in Phase 1 and 2 of the Cotton Valley Imaging Project. Overall, we can surmise that the source parameter distributions suggest that each and every treatment resulted in differences in fracture growth and behaviour. Variations, particularly in E_s/E_p ratio, appear to provide insight into the propped volumes rather than just the overall fracture dimensions as defined by event locations. In this context, it can be suggested that the Phase 1 treatments were likely more effective in creating propped volumes than the Phase 2 treatments. Regional differences in magnitude, apparent stress, and b-values generally outlined zones where failures occurred under increased effective stress levels, which tended to coincide with increased E_s/E_p levels. It can be considered that these correlations can be used to define regions of the fracture where fracture growth is occurring but not necessarily contributing to the development of the propped zone. Additionally, it appears that these apparent non-propped zones occur during the late stages of fracture development, after the propped zone has been created.

References

- Aki, K. and Richards, P.G., 1980, Quantitative seismology, theory and methods, volume 2. W.H. Freeman and Co., San Francisco.
- Andrews, D.J. (1986). Objective determination of source parameters and similarity of earthquakes of different sizes, in *Earthquake Source Mechanics*, S. Das, J. Boatwright, and C. H. Scholz (eds.), Am. Geophys. Union, Washington, D.C., 259-267.
- Boore D.M. and J. Boatwright (1984). Average body-wave radiation coefficients, *Bull. Seismol. Soc. Am.*, 74, 1615-1621.
- Brune, J. N. (1970). Tectonic stress and the spectra of seismic shear waves from earthquakes, *J. Geophys. Res.* 75, 4997-5009. Correction in *J. Geophys. Res.*, 76, 5002, 1971.
- Flinn, E.A., 1965, Signal analysis using rectilinearity and direction of particle motion, *Proc. I.E.E.E.*, 53, 1725-1743.
- Hill, D.P., 1977, A model for earthquake swarms, *J. Geophys. Res.*, 82, 347-352.
- Madariaga, R. (1976). Dynamics of an expanding circular fault, *Bull. Seismol. Soc. Am.*, 66, 639-666.
- Pinnacle Technologies, Inc., 1999, Cotton Valley Fracture Imaging Project Phase III, Final Report for JIP Consortium, 68p, July 9, 1999.
- Rutledge, J.T., 1998, Analyses of the Cotton Valley microseismic data for asymmetric fracture growth, Report to the Gas Research Institute, July, 1998.
- Rutledge, J.T., Phillips, W.S., House, L.S., Zinno, R.J., 1998, Microseismic mapping of a Cotton Valley hydraulic fracture using decimated downhole arrays, 68th Ann. Mtg., Soc. of Explor. Geophys., 338-341.
- Sato, H. (1984). Attenuation and envelope formation of three-component seismograms of small local earthquakes in randomly inhomogeneous lithosphere, *J. Geophys. Res.*, 89, 1221-1241.
- Sibson, R.H., 1996, Structural permeability of fluid-driven fault-fracture meshes, *J. Structural Geol.*, 18, 1031-1042.
- Snoke, J.A. (1987). Stable determination of (Brune) stress drops, *Bull. Seismol. Soc. Am.*, 77, 530-538.
- Urbancic, T.I, C-I. Trifu, R.A. Mercer, A.J. Feustel, and J.A.G. Alexander (1996). Automatic time-domain calculation of source parameters for the analysis of induced seismicity, *Bull. Seismo. Soc. Am.*, 86, 1627-1633.
- Urbancic, T.I. and C-I. Trifu (1997). Seismic monitoring of mine environments, in *Proceedings of Exploration 97: Fourth Decennial International Conference on Mineral Exploration* (ed. A.G. Gubins), Toronto, September 14-18, 1997, 941-950.
- Urbancic, T.I., 1998, Cotton Valley hydraulic fracture imaging project: Phase II (CGU21-9) Fracture imaging using microearthquake event locations, Engineering Seismology Group Canada Report ESG98-11, Report to the Gas Research Institute, June, 1998.
- Urbancic, T.I., and Zinno, R.J., 1998, Cotton Valley Hydraulic Fracture Imaging Project: Feasibility of determining fracture behavior using microseismic event locations and source parameters, 68th Ann. Mtg., Soc. of Explor. Geophys., 964-967.

- Urbancic, T.I., Shumila, V., Rutledge, J.T., and Zinno, R.J., 1999, Determining hydraulic fracture behavior using microseismicity, Proceedings of the 37th U.S. Rock Mechanics Symposium, 991-997, Vail, Colorado, U.S.A., June 6-9.
- Walker, Jr., R.N., 1997, Cotton Valley Hydraulic Fracture Imaging Project: SPE paper 38577, presented at the 1997 Soc. Petrol. Eng. Annual Technical Conference and Exhibition, San Antonio, Texas.
- Warpinski, N.R., et al., 1997, A Re-Analysis of The Cotton Valley Hydraulic Fracture Imaging Project: Imaged Geometry of the Taylor Sand Hydraulic Fractures, GRI Diagnostic Project Team, December, 1997.
- Withers, R.J. and Dart, R.P., 1997a, Cotton Valley Production Stimulation Hydrofracture Microseismic Monitoring & Imaging, Data Collection and Analysis Report, ARCO Exploration & Production Technology, June, 1997.
- Withers, R.J. and Dart, R.P., 1997b, Cotton Valley Production Stimulation Hydrofracture Microseismic Monitoring & Imaging, Phase II (CGU2109 Fracture Imaging), Data Collection and Analysis Report, ARCO Exploration & Production Technology, July, 1997.

Cotton Valley Phase IV

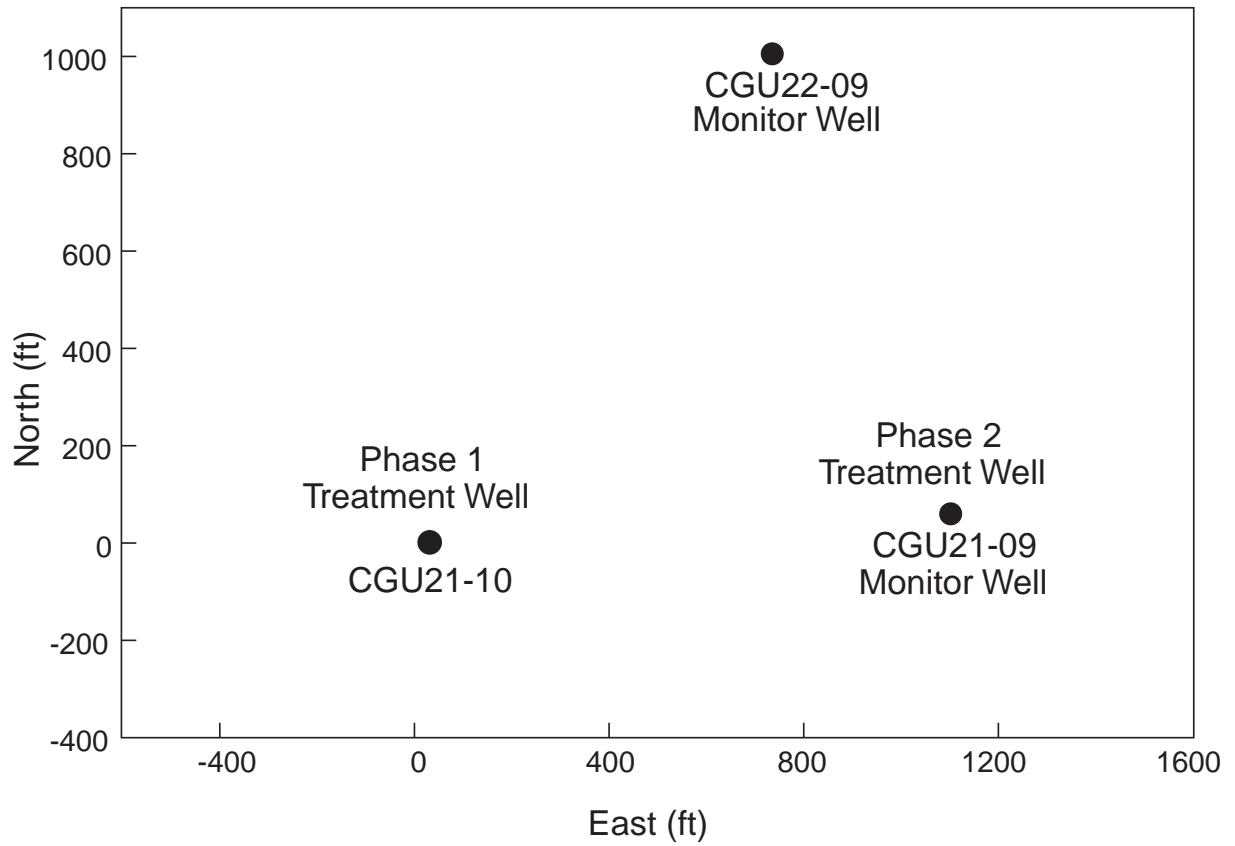


Figure 1. Wells used in Phase 1 and 2.

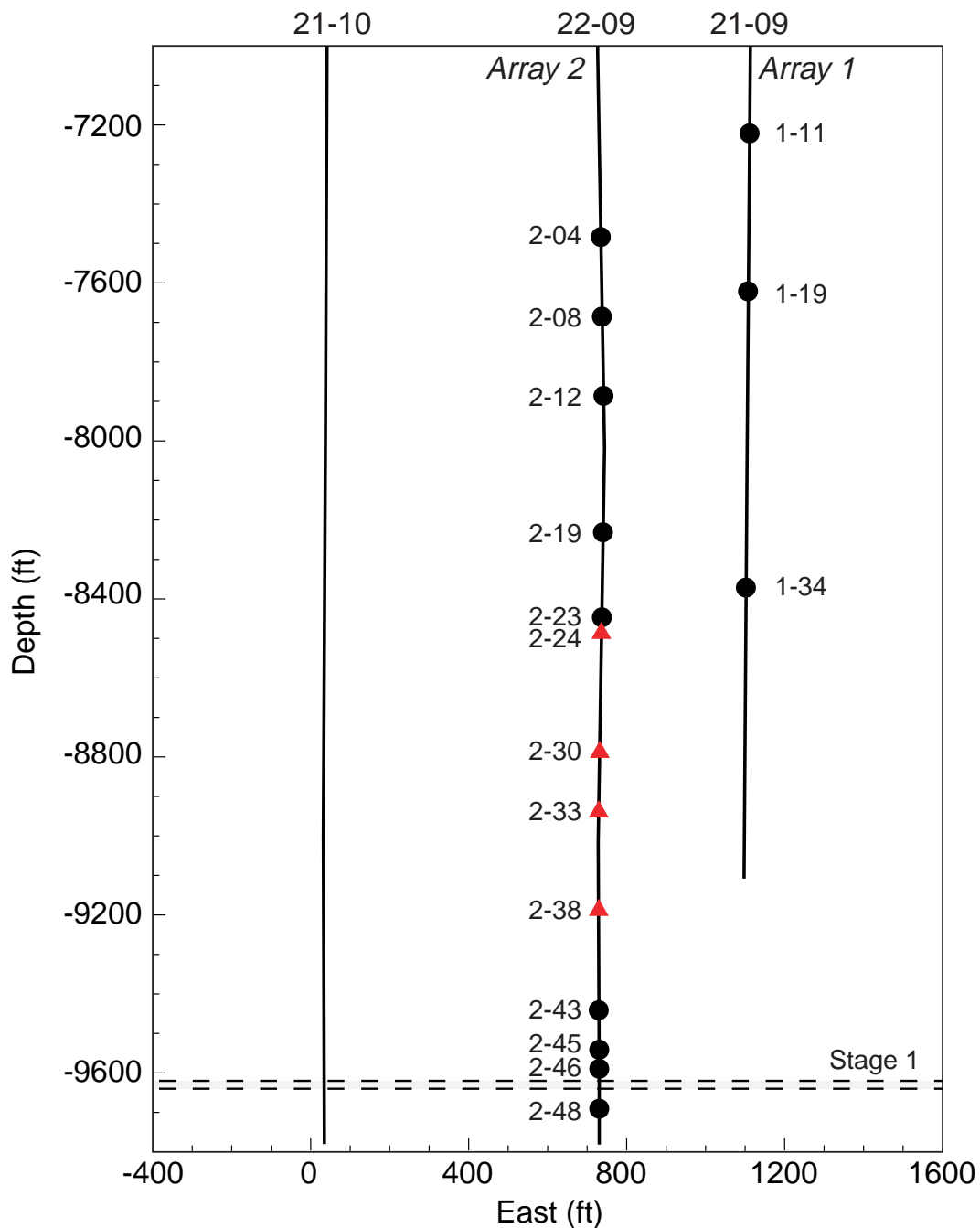


Figure 2. Subset of receiver stations used for Phase-1, Stage-1 (Taylor Sand) mapping. Red triangle stations provided horizontal-component hodogram data as well as travelttime data. For most events, array 1 only provided S-wave arrival time at station 1-34. Dashed lines mark the perforated depth interval.

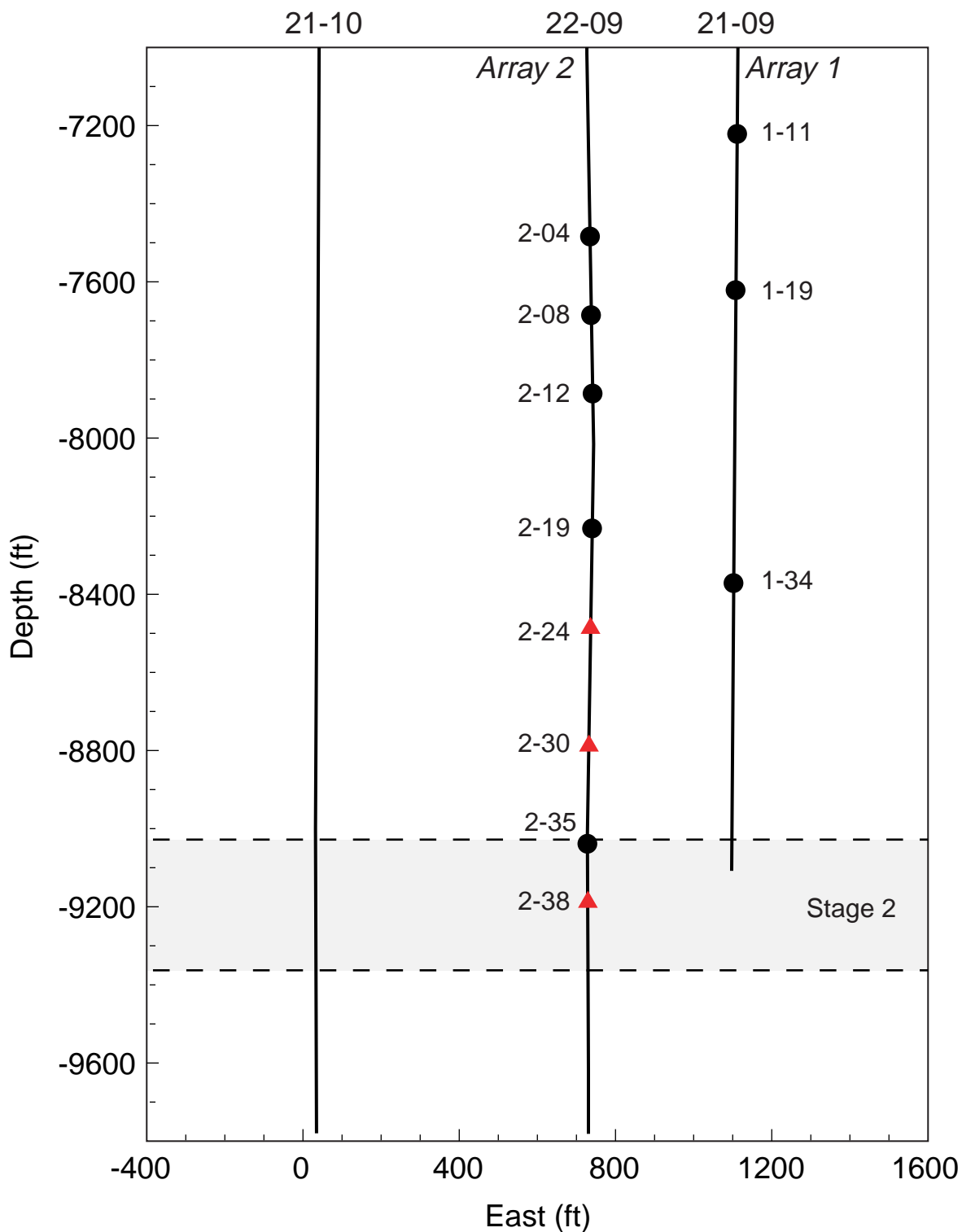


Figure 3. Subset of receiver stations used for Phase-1, Stage-2 mapping. Red triangle stations provided horizontal-component hodogram data as well as traveltimes data. Dashed lines mark the perforated depth interval.

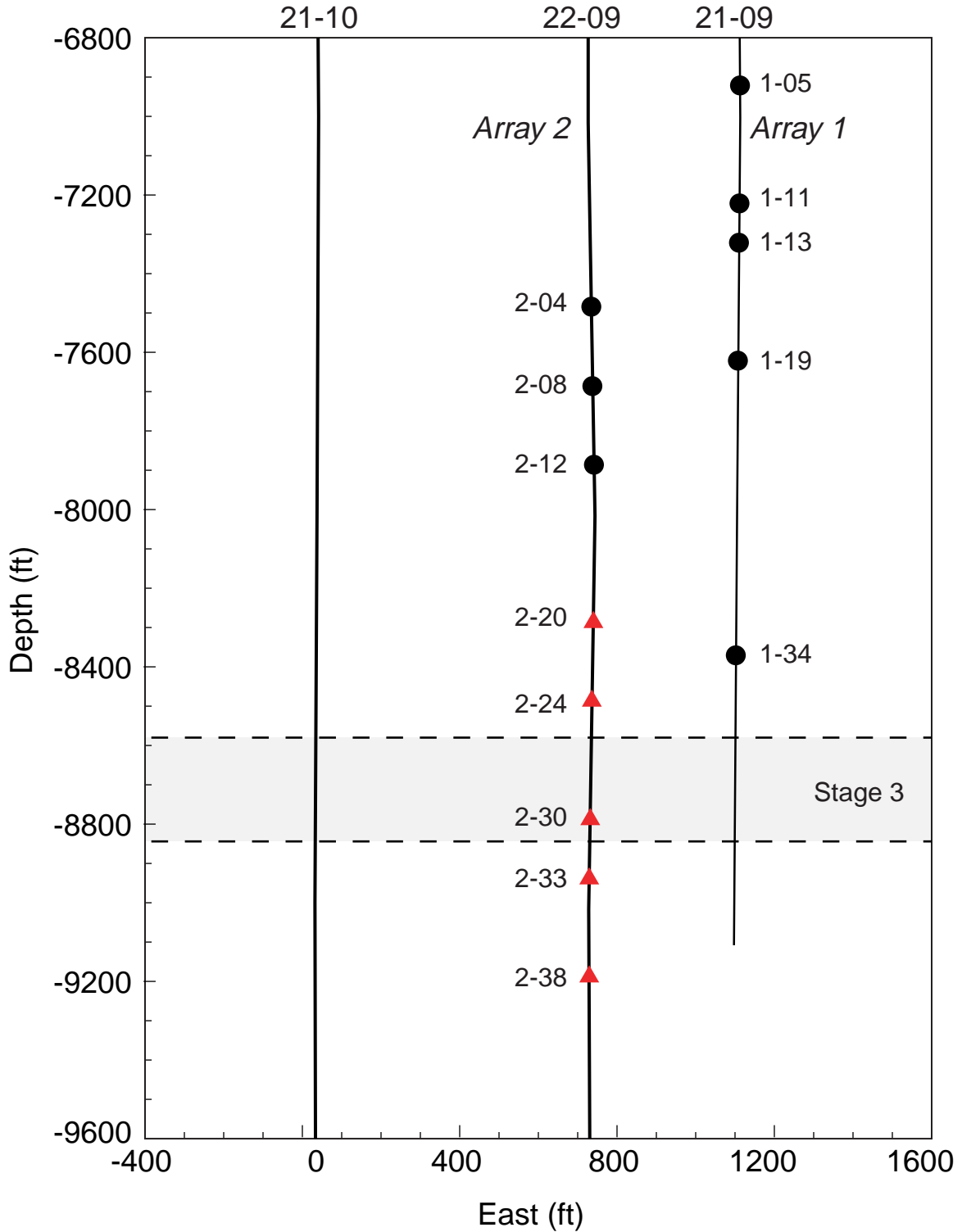


Figure 4. Subset of receiver stations used for Phase-1, Stage-3 mapping. Red triangle stations provided horizontal-component hodogram data as well as traveltimes. Dashed lines mark the perforated depth interval.

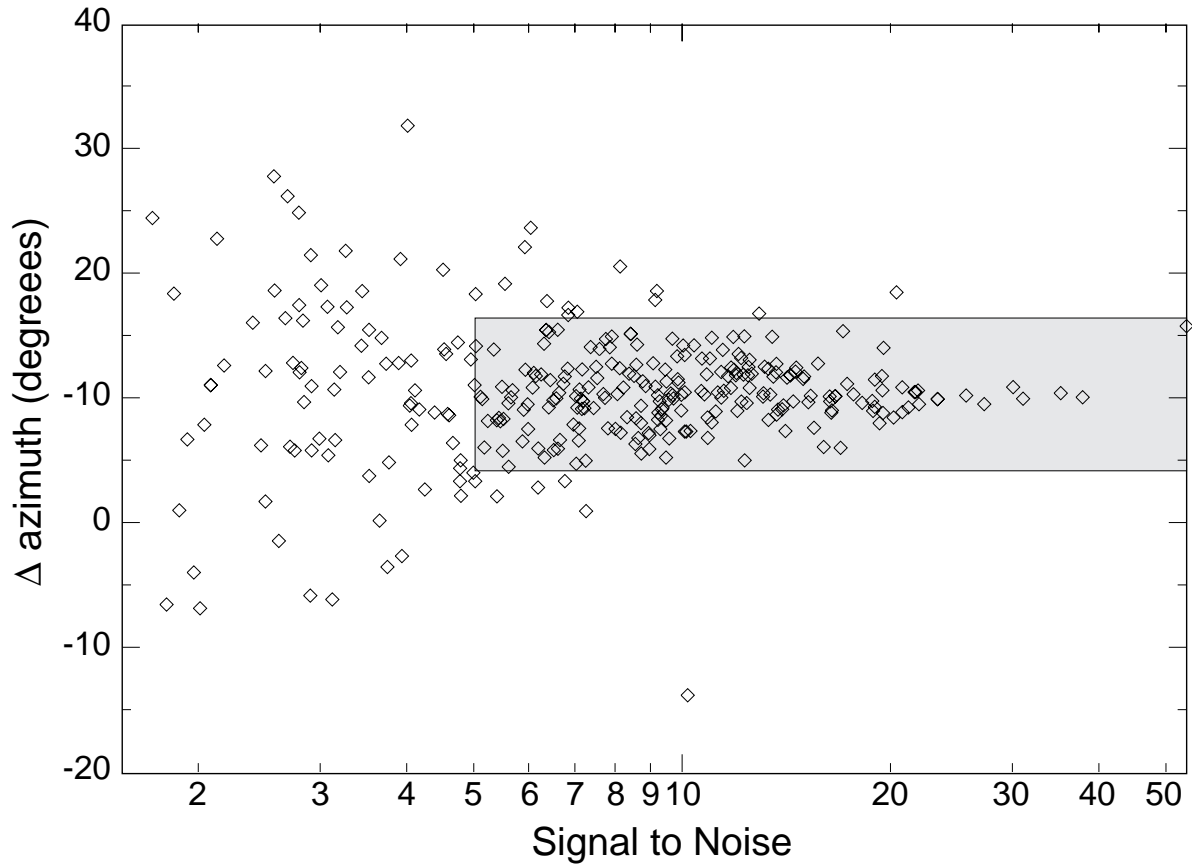


Figure 5. Scatter plot of P-wave hodogram azimuthal difference for a set of Phase-1, Stage-2 microearthquakes as a function of first arrival signal-to-noise ratio (Stations 2-30 minus 2-38). Selection criteria for the use of hodogram data falls within the shaded area ($S/N \geq 5$ and $\Delta \text{azimuth} \leq \pm 6^\circ$ from the median difference). Standard deviation within the shaded area is about $\pm 3^\circ$. Median $\Delta \text{azimuth}$ values provide a robust measure of relative sonde orientations.

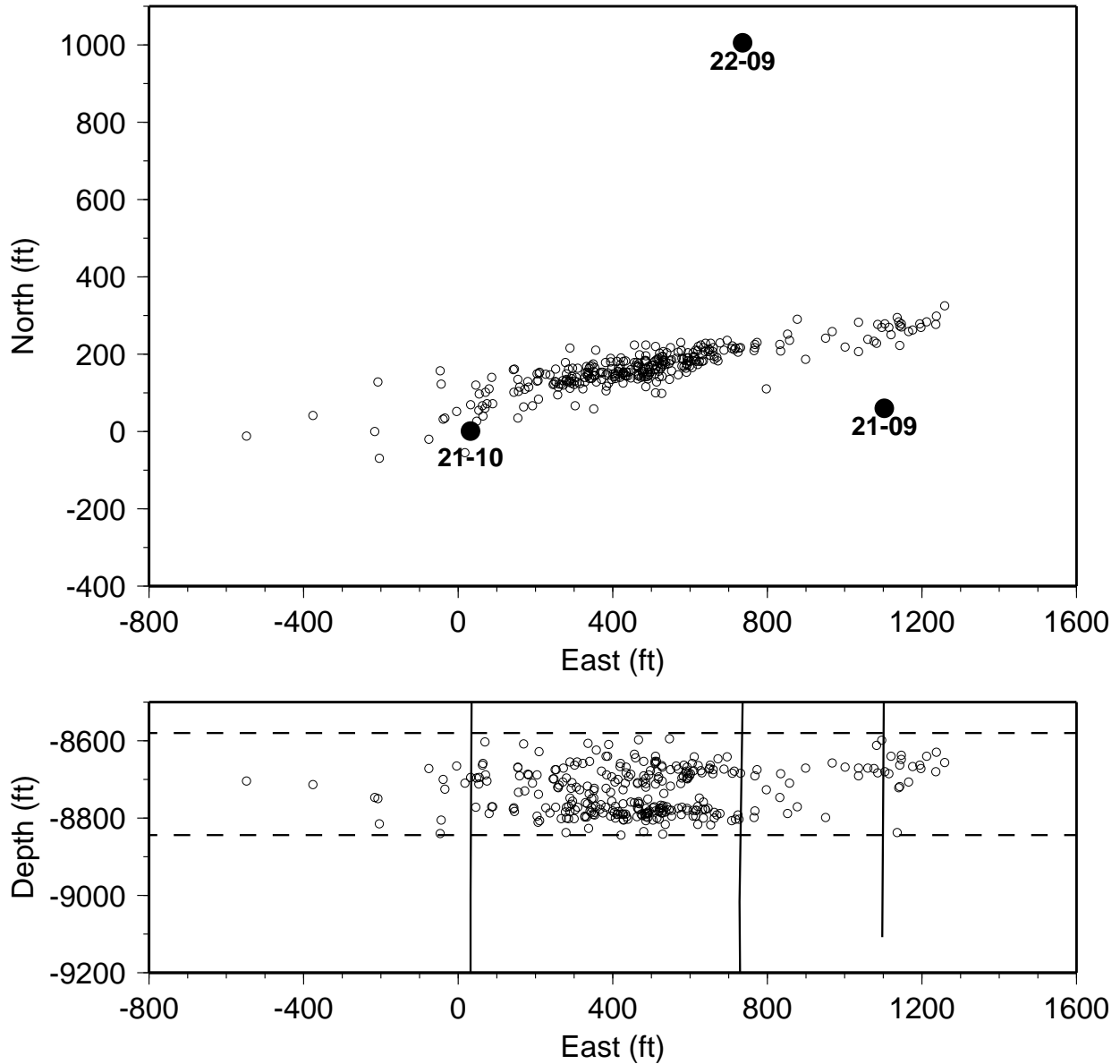


Figure 6. A subset of Phase-1, Stage-3 event locations using JHD and a log-based velocity model (Figure 7). The subset are the highest quality, in-zone locations based on 2-well arrival-time data, multiple hodogram data, and low residuals (misfit of predicted and observed data). This subset of events were then used to calibrate final velocity model used for the entire Phase-1, Stage-3 data set. Datum is Kelly Bushing (K.B.) of well 21-10.

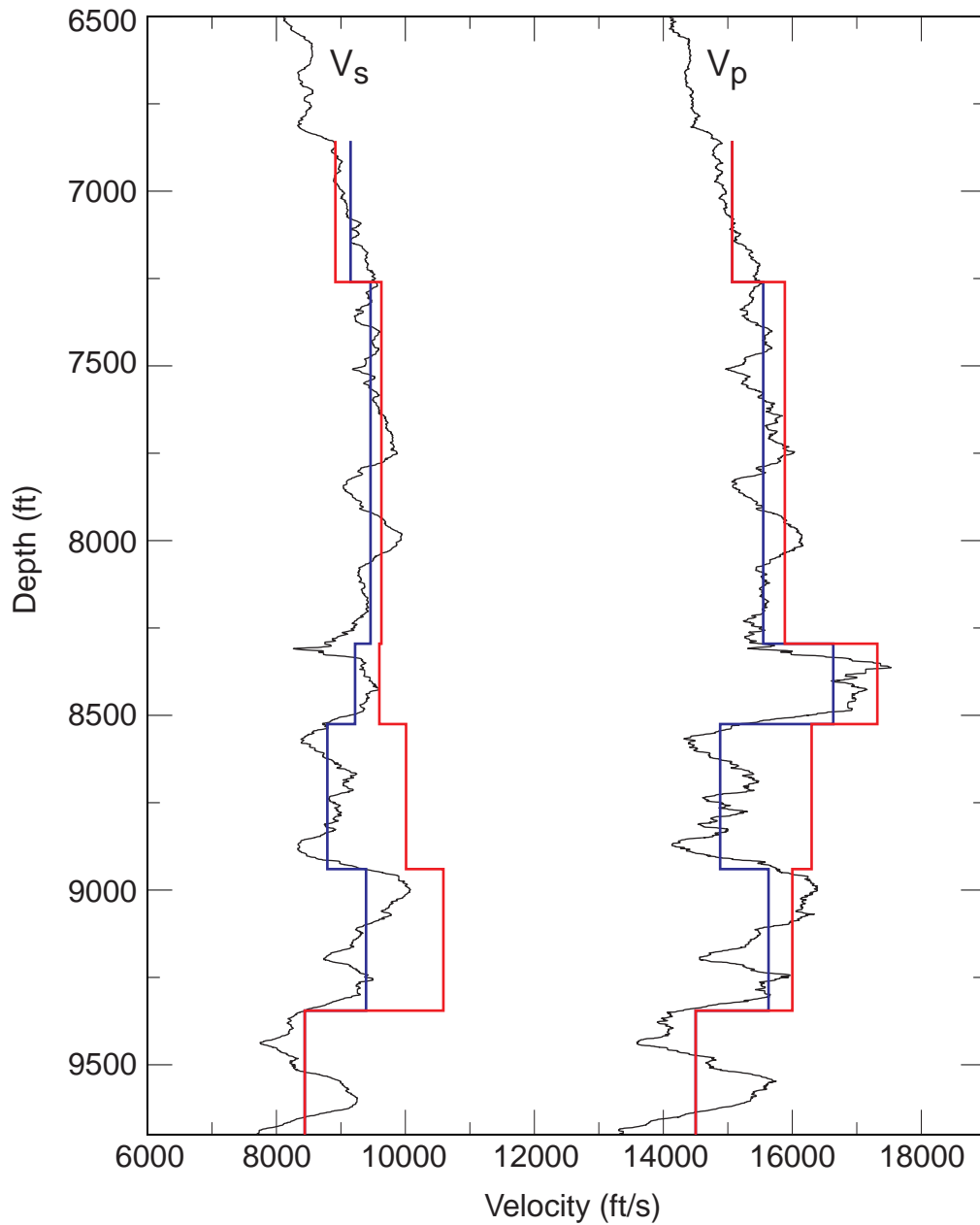


Figure 7. Smoothed sonic logs and 6-layer velocity model based on log interval averages (blue). The Phase-1, Stage-3 velocity model inversion results are shown in red. Red overlays the starting model (blue) in layers with no travel paths (no change in model). The sonic-log data from wells 21-10 and 21-09 were smoothed with a 100-ft moving, median window, then shifted for alignment, and then summed and averaged.

Phase 1, Stage 1, 05/12/97 Frac

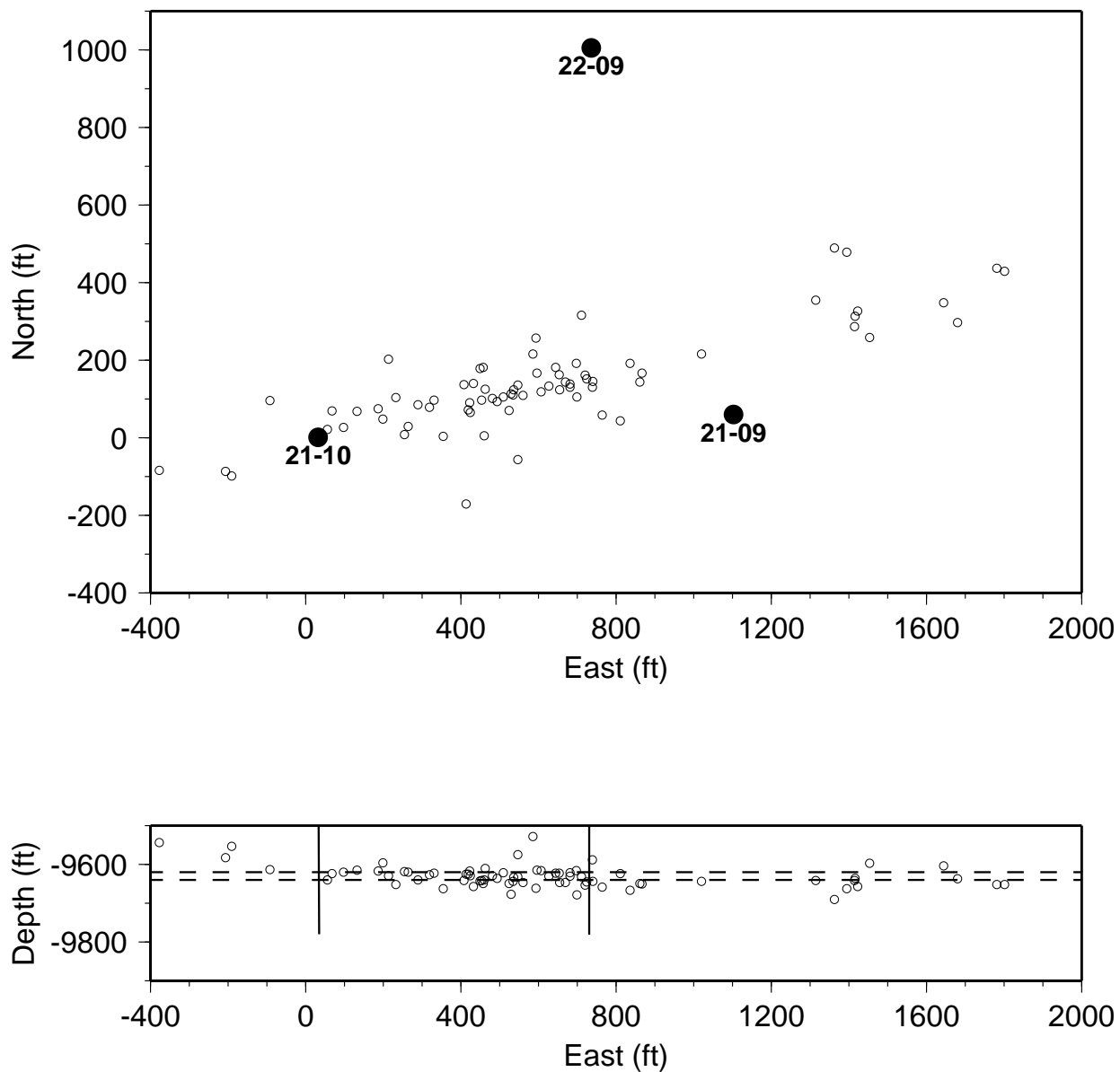


Figure 8. Phase-1, Stage-1 event locations. Perforated depth interval is marked with dashed lines. Datum is K.B. of 21-10.

Phase 1, Stage 1, 05/12/97 Frac

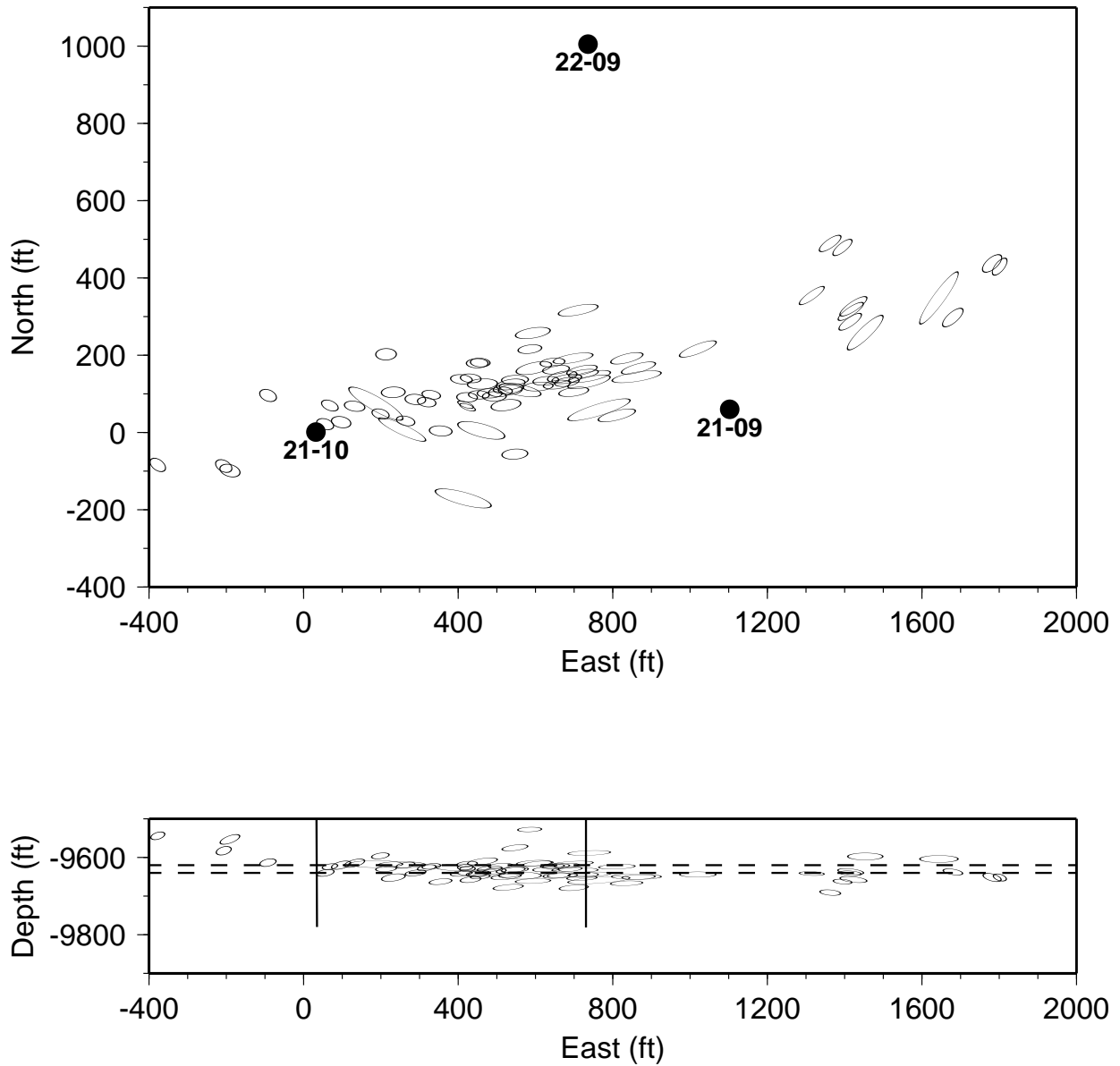


Figure 9. Phase-1, Stage-2 error ellipsoids projections. Single-well locations are evident from the longer ellipses in map view, oriented orthogonal to the trajectory from monitor well 22-09. The median principal error axes is ± 33 ft.

Phase 1, Stage 2, 05/14/97 Frac

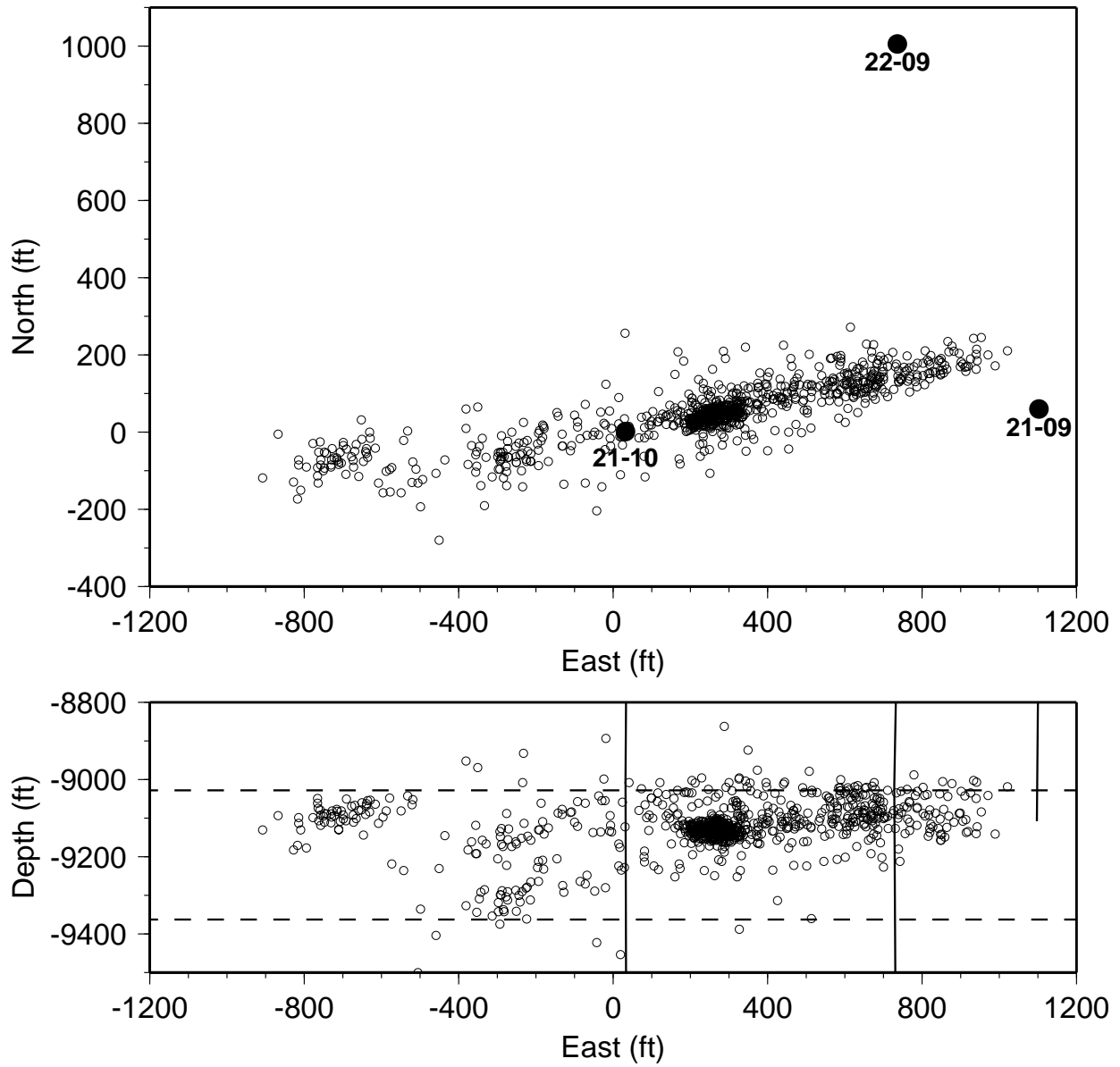


Figure 10. Phase-1, Stage-2 locations. Datum is K.B. of 21-10.

Phase 1, Stage 2, 05/14/97 Frac

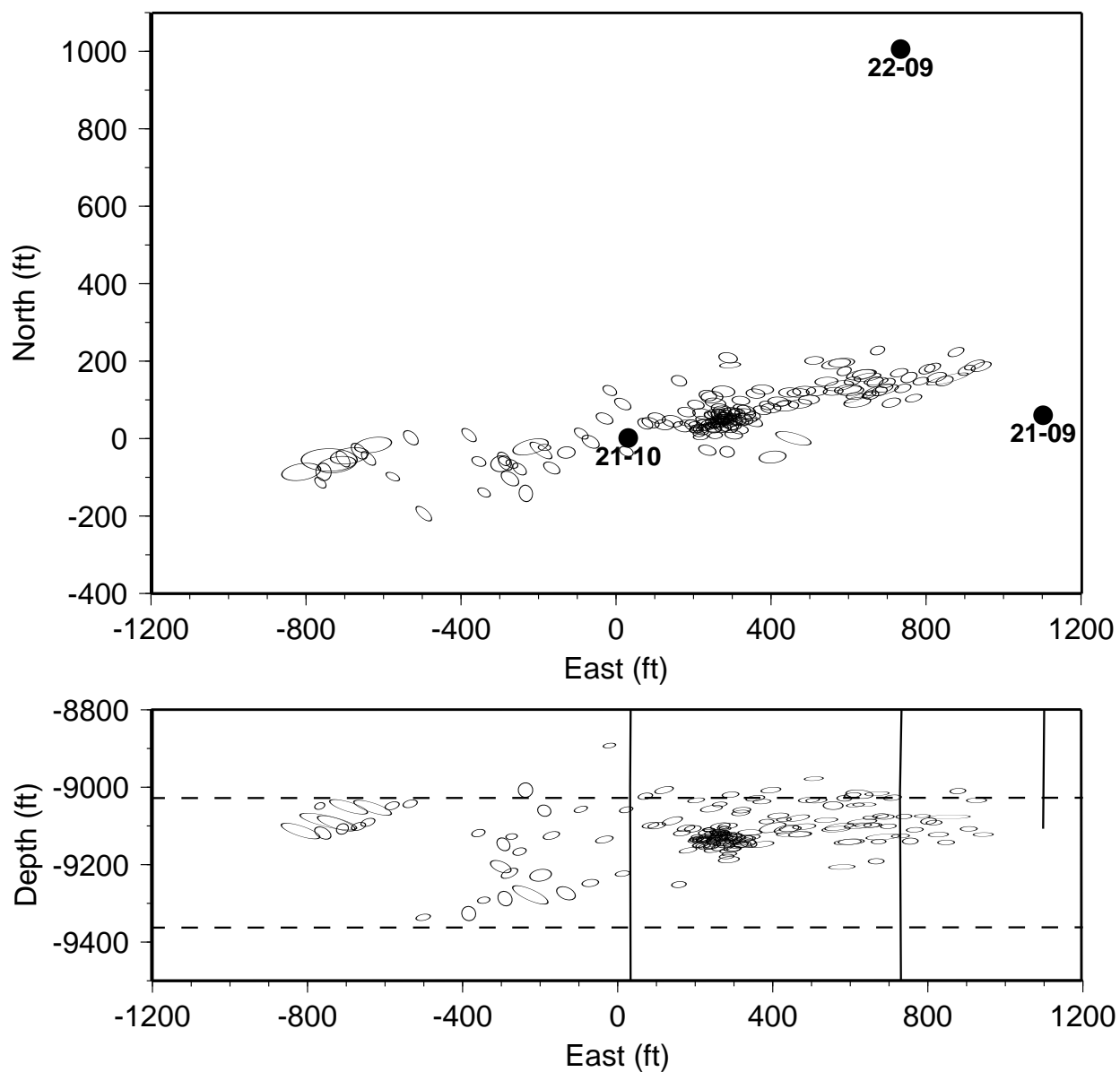


Figure 11. Phase-1, Stage-2 error ellipsoids projections. Every 5th error ellipsoid is shown to reduce overprinting, after sorting events from west to east. The median principal error axes is ± 21 ft.

Phase 1, Stage 3, 05/16/97 Frac

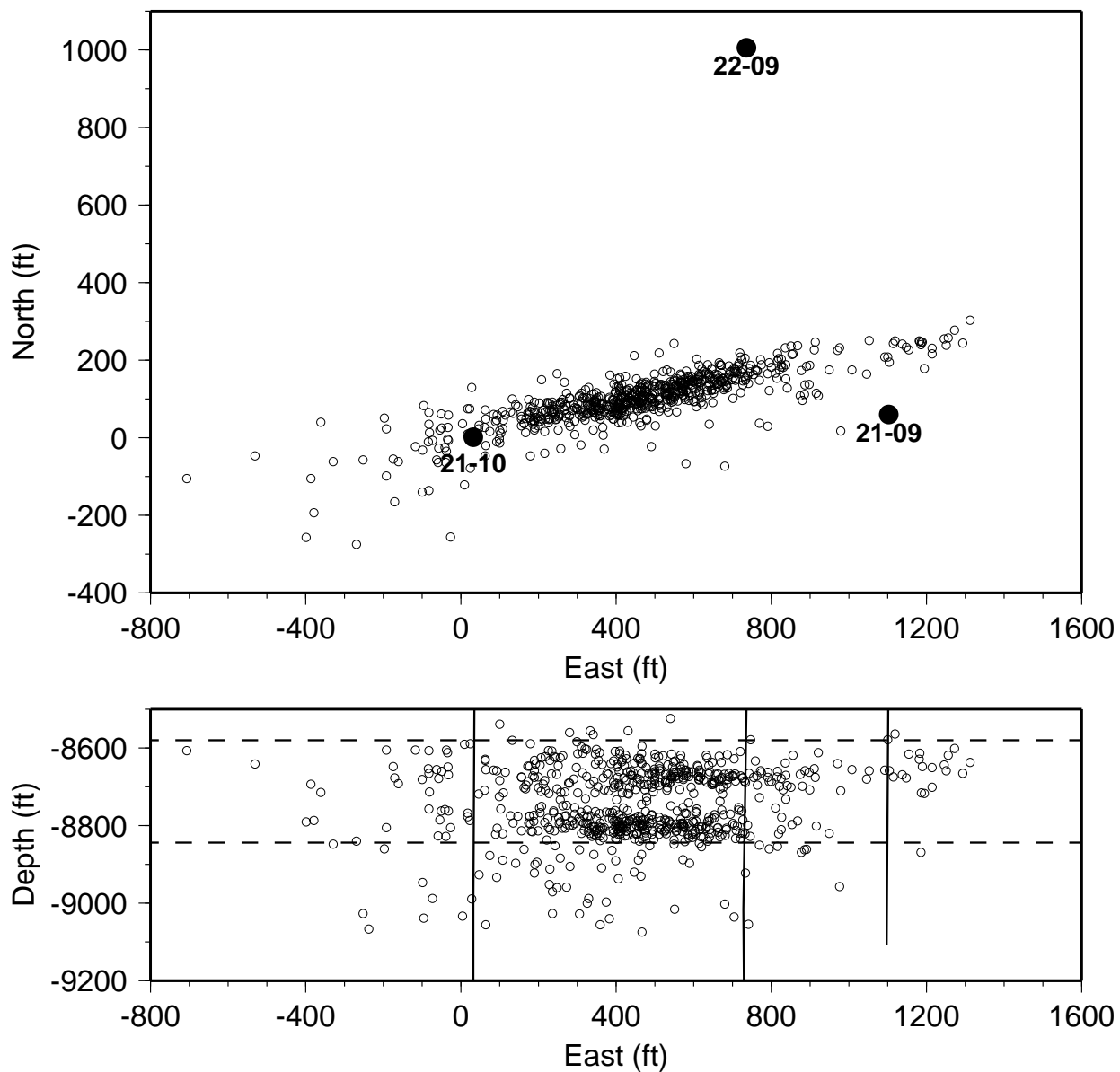


Figure 12. Phase-1, Stage-3 locations. Datum is K.B. of 21-10.

Phase 1, Stage 3, 05/16/97 Frac

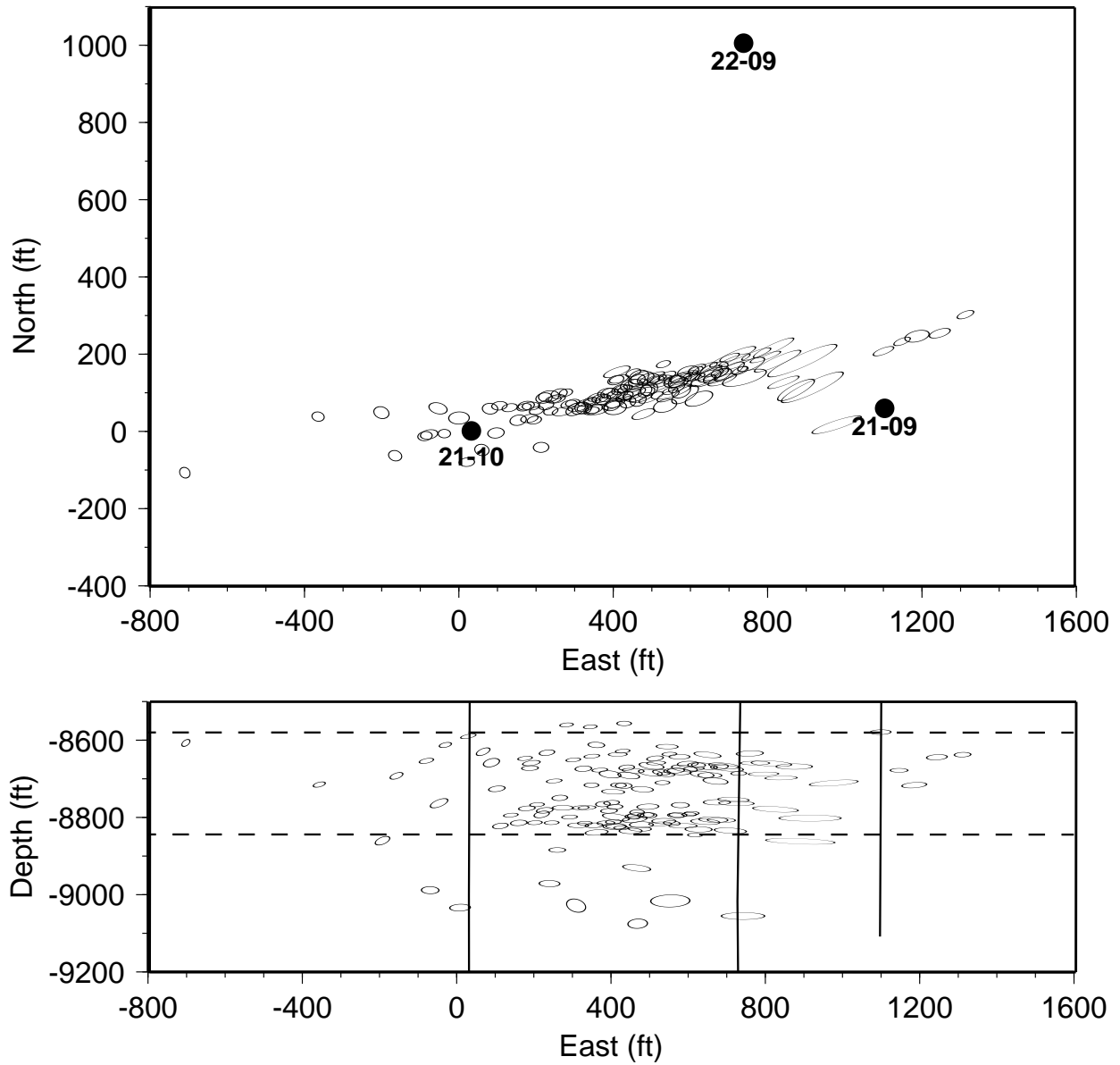


Figure 13. Phase-1, Stage-3 error ellipsoids projections. Every 5th error ellipsoid is shown to reduce overprinting, after sorting events from west to east. The median principal error axes is ± 25 ft.

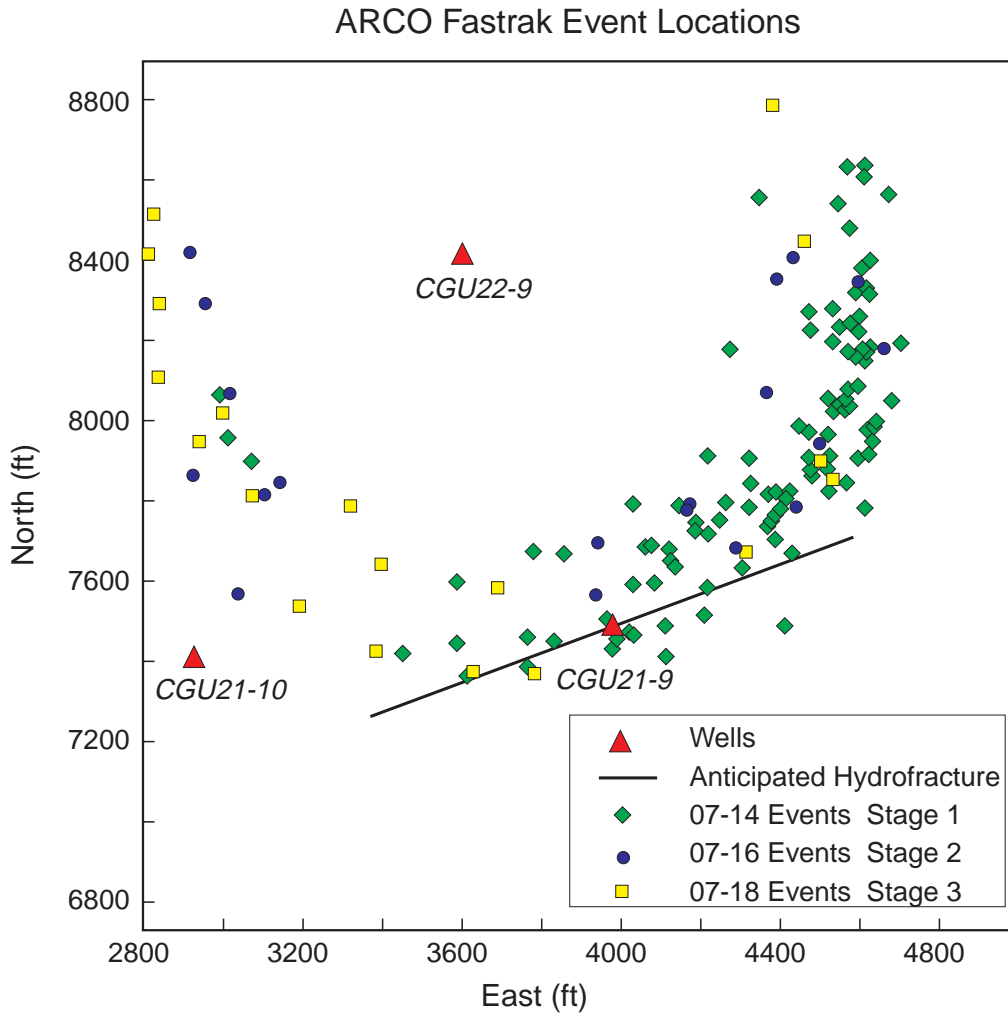


Figure 14. ARCO's locations determined for small subsets of the Phase-2 (CGU21-9) treatments. The arcing pattern about the monitor well (CGU22-9) indicates a problem with the hodogram (azimuthal) data.

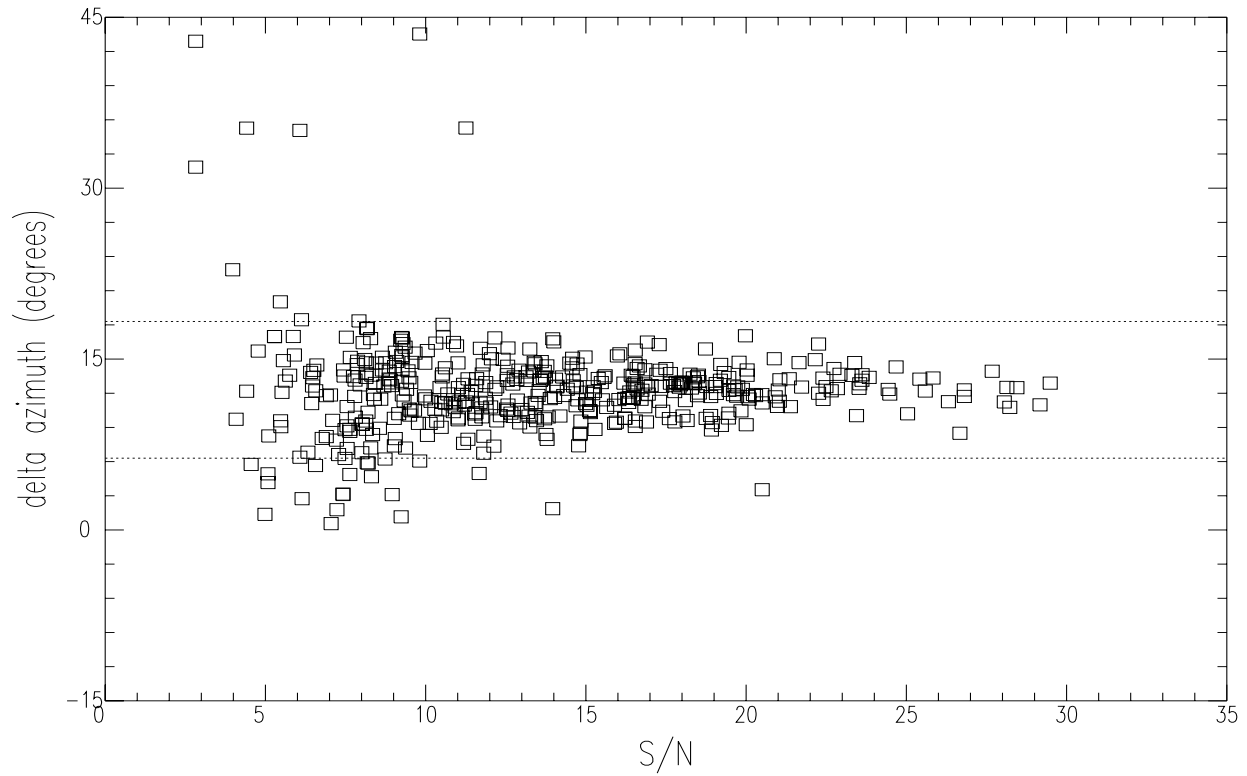


Figure 15. Scatter plot of S-wave hodogram azimuthal difference for a set of Phase-2, Stage-1 microearthquakes as a function of S-wave first arrival signal-to-noise ratio (Stations 2-30 minus 2-24). Comparison with P-wave data (e.g. Figure 5) shows that the S-wave azimuthal data have less scatter (smaller error) and a much higher percentage of events that meet the selection criteria ($S/N \geq 5$ and $\Delta\text{azimuth} \leq \pm 6^\circ$ from the median difference). Standard deviation within the $\pm 6^\circ$ bounds is about $\pm 2.5^\circ$.

Cotton Valley Phase IV

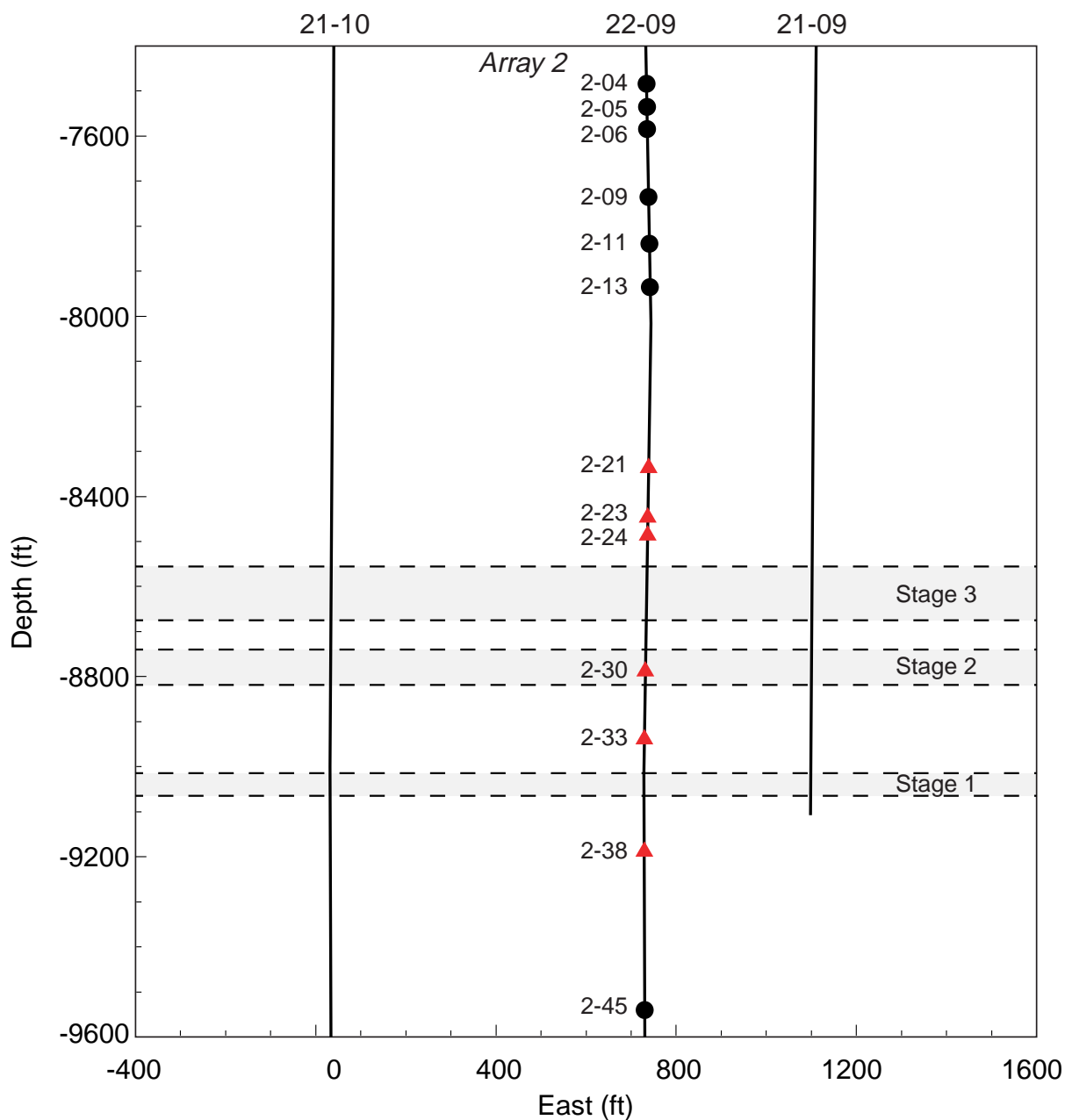


Figure 16. Subset of receiver stations used for Phase-2 mapping. Red triangle stations provided horizontal-component hodogram data as well as travelttime data. Dashed lines mark the perforated depth intervals of the 3 completion stages.

Phase 2, Stage 1, 07/14/97 Frac

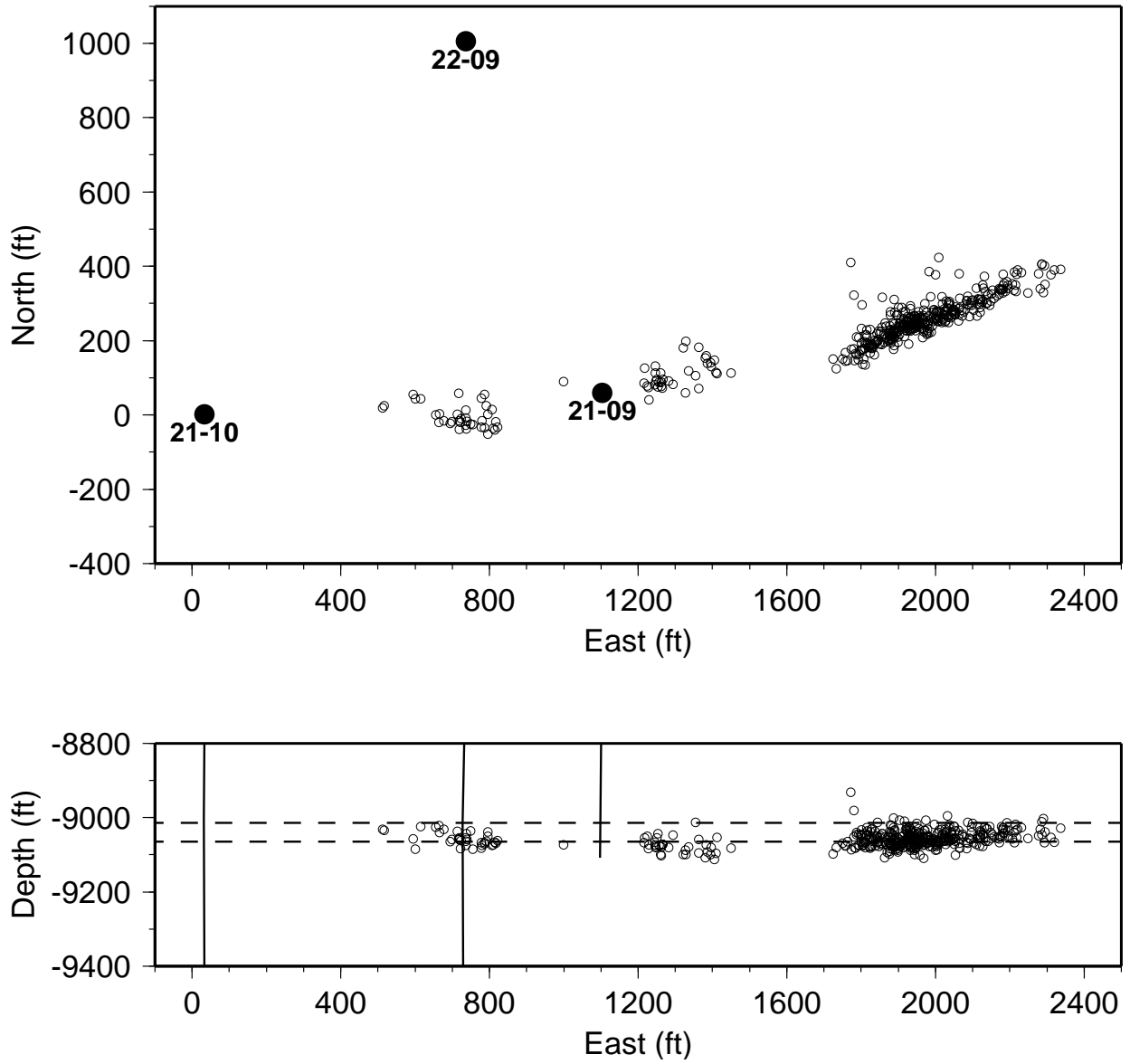


Figure 17. Phase 2, Stage-1 locations. Datum is K.B. of 21-10. The perforated depth interval is marked with dashed lines.

Phase 2, Stage 1, 07/14/97 Frac

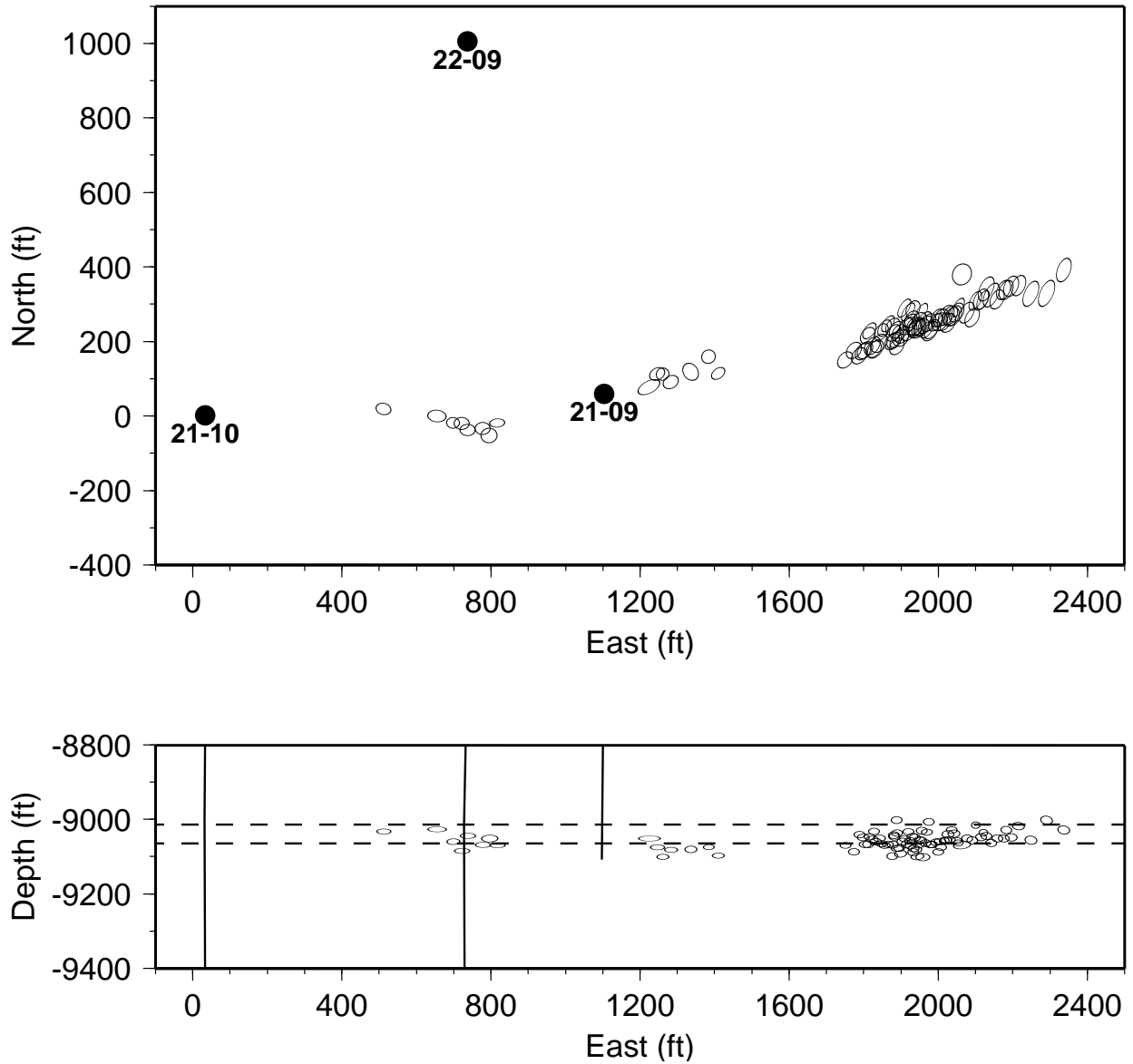


Figure 18. Phase-2, Stage-1 error ellipsoids projections. Every 5th error ellipsoid is shown to reduce overprinting, after sorting events from west to east. The median principle error axes is ± 25 ft.

Phase 2, Stage 2, 07/16/97 Frac

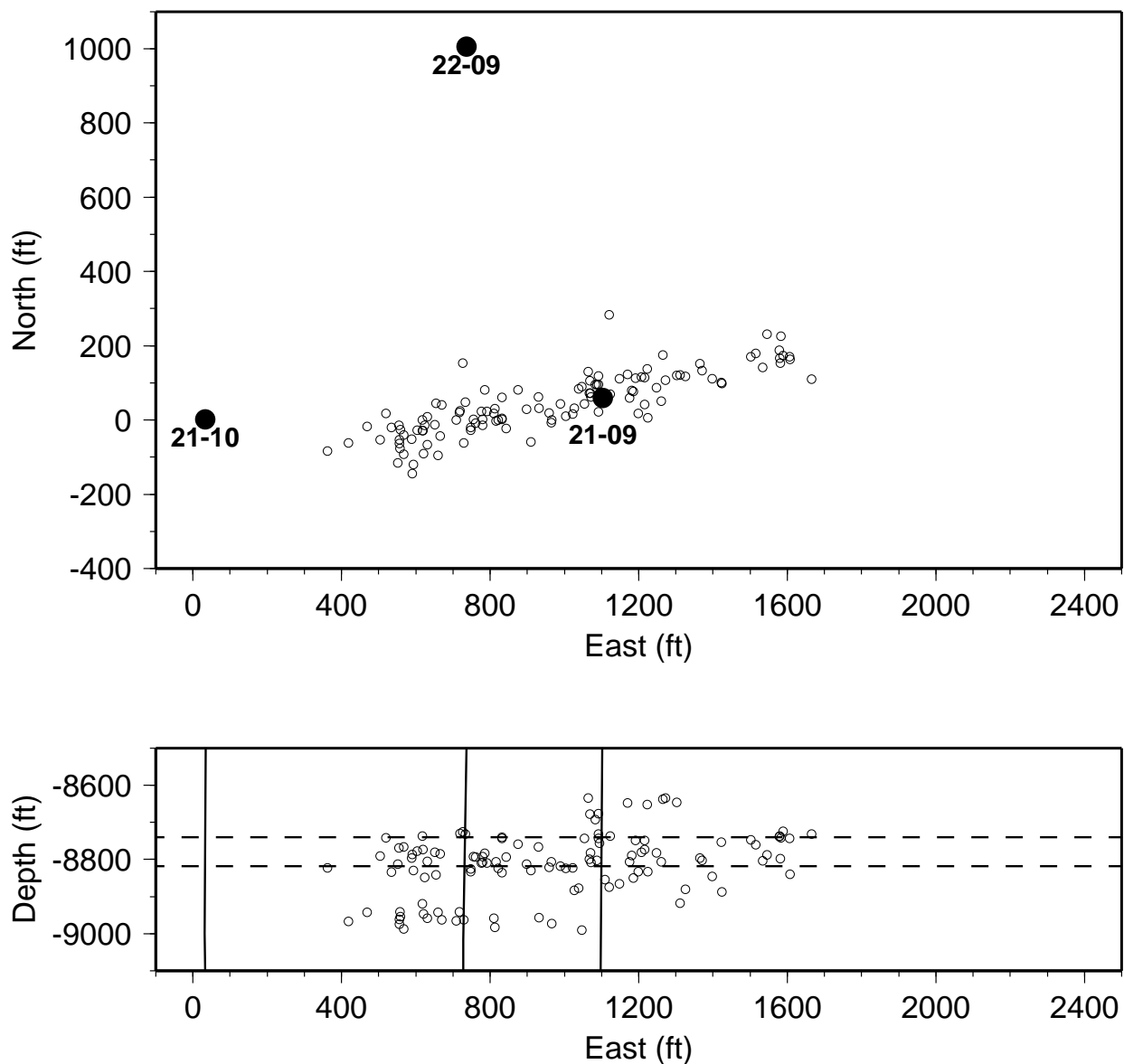


Figure 19. Phase 2, Stage-2 locations. Datum is K.B. of 21-10.

Phase 2, Stage 2, 07/16/97 Frac

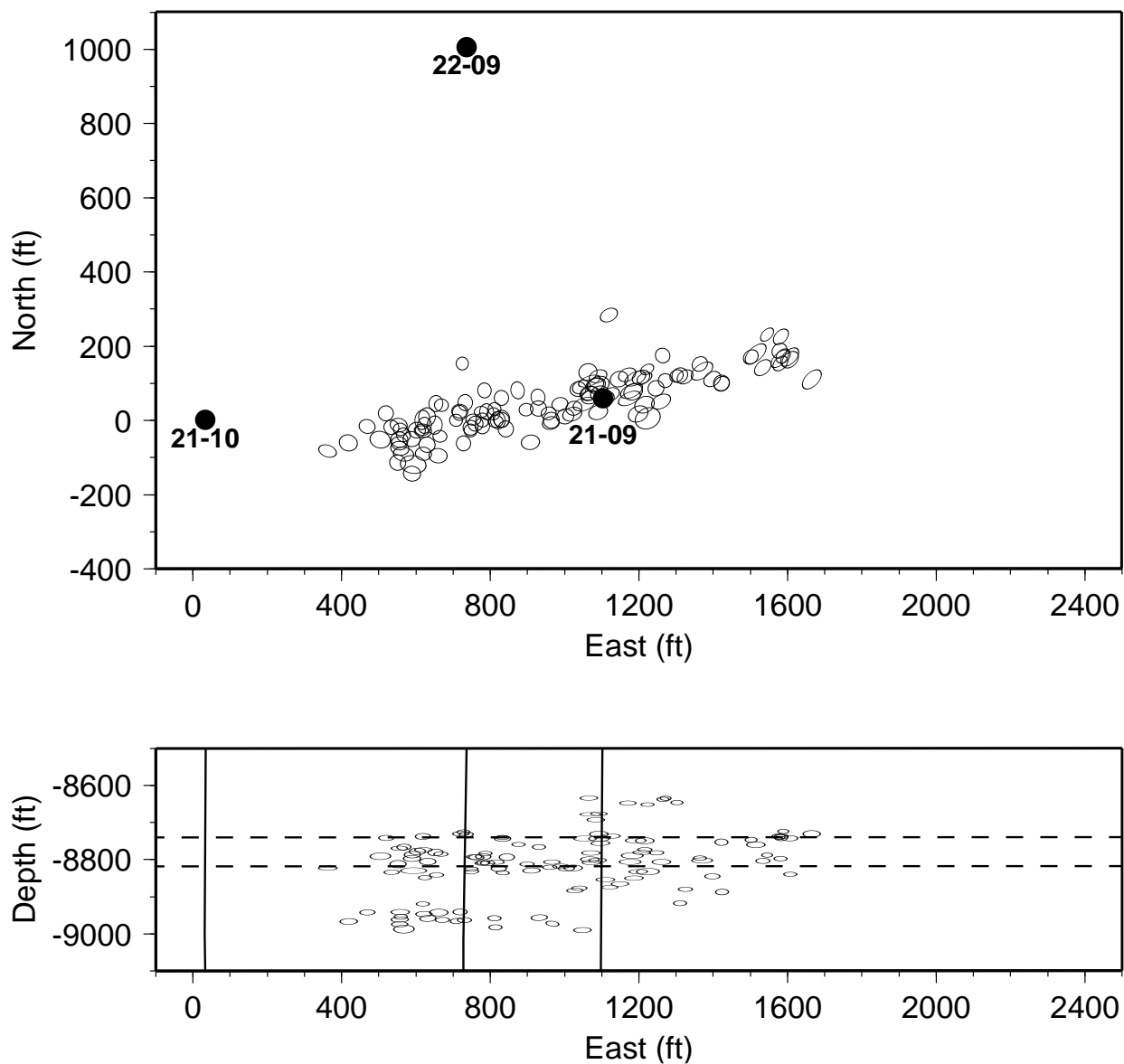


Figure 20. Phase-2, Stage-2 error ellipsoids projections. The median principle error axes is ± 23 ft.

Phase 2, Stage 3, 07/18/97 Frac

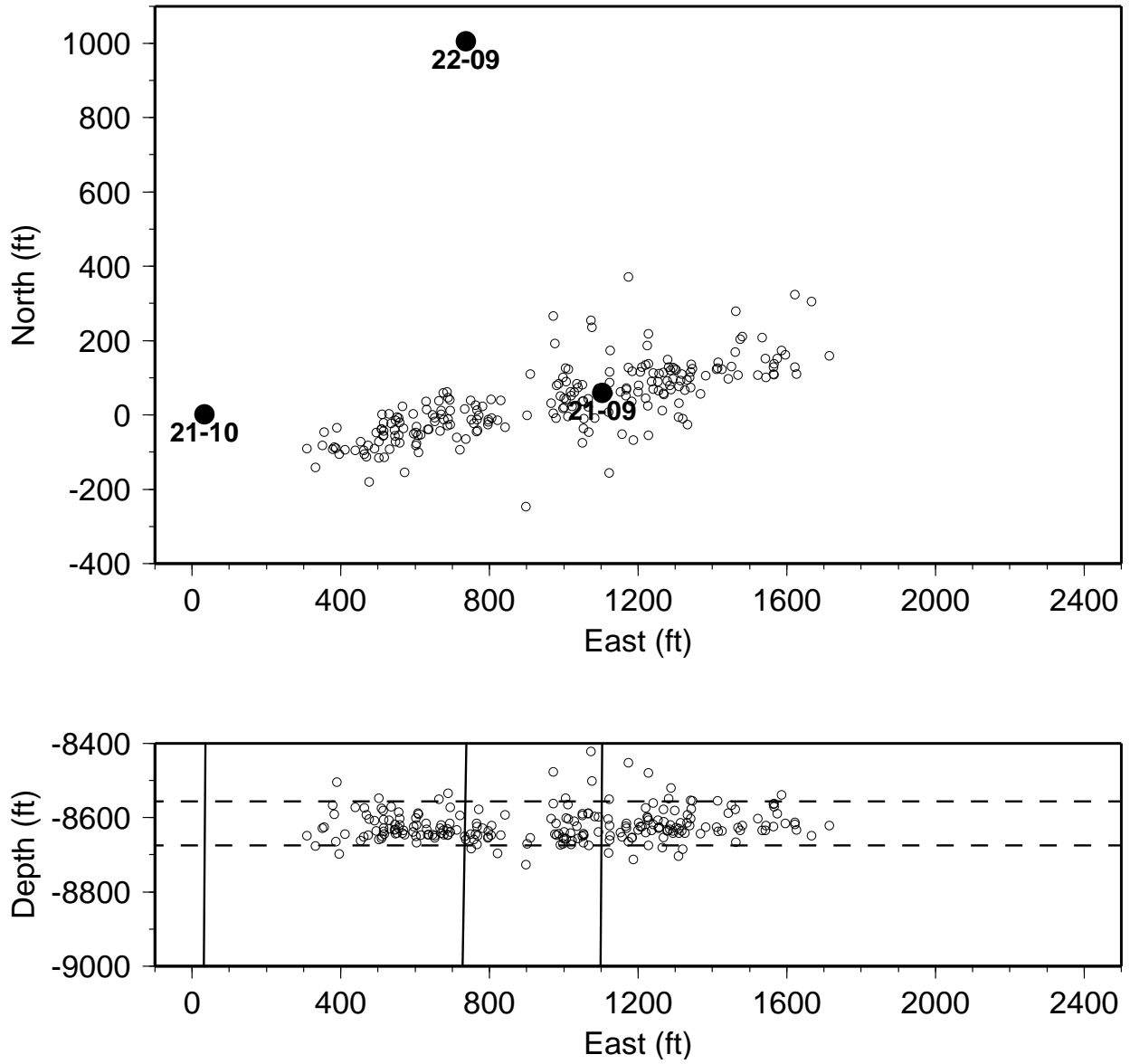


Figure 21. Phase 2, Stage-3 locations. Datum is K.B. of 21-10.

Phase 2, Stage 3, 07/18/97 Frac

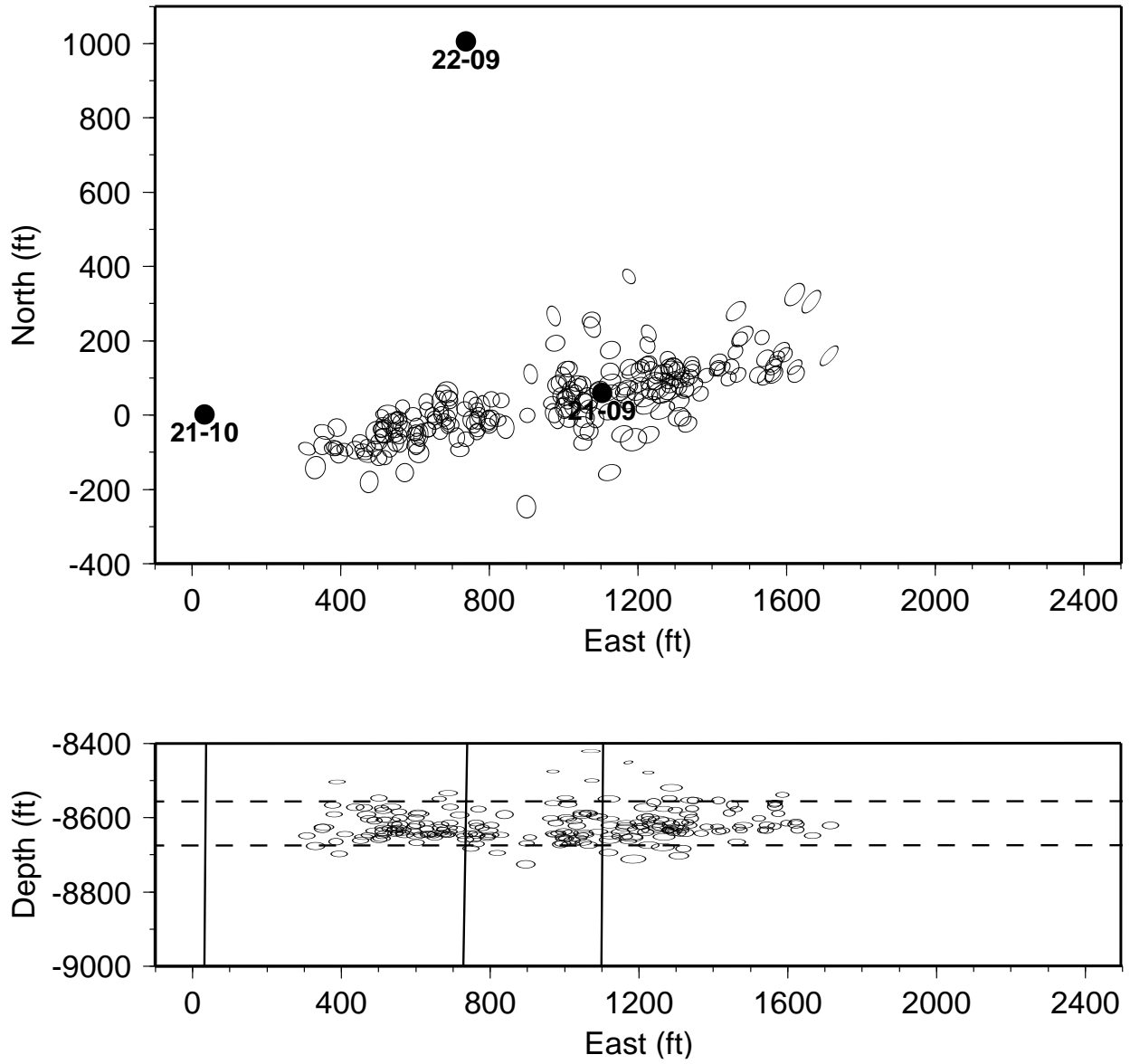


Figure 22. Phase-2, Stage-3 error ellipsoids projections. The median principle error axes is ± 24 ft.

Phase 1, 0512 Hydraulic Fracture

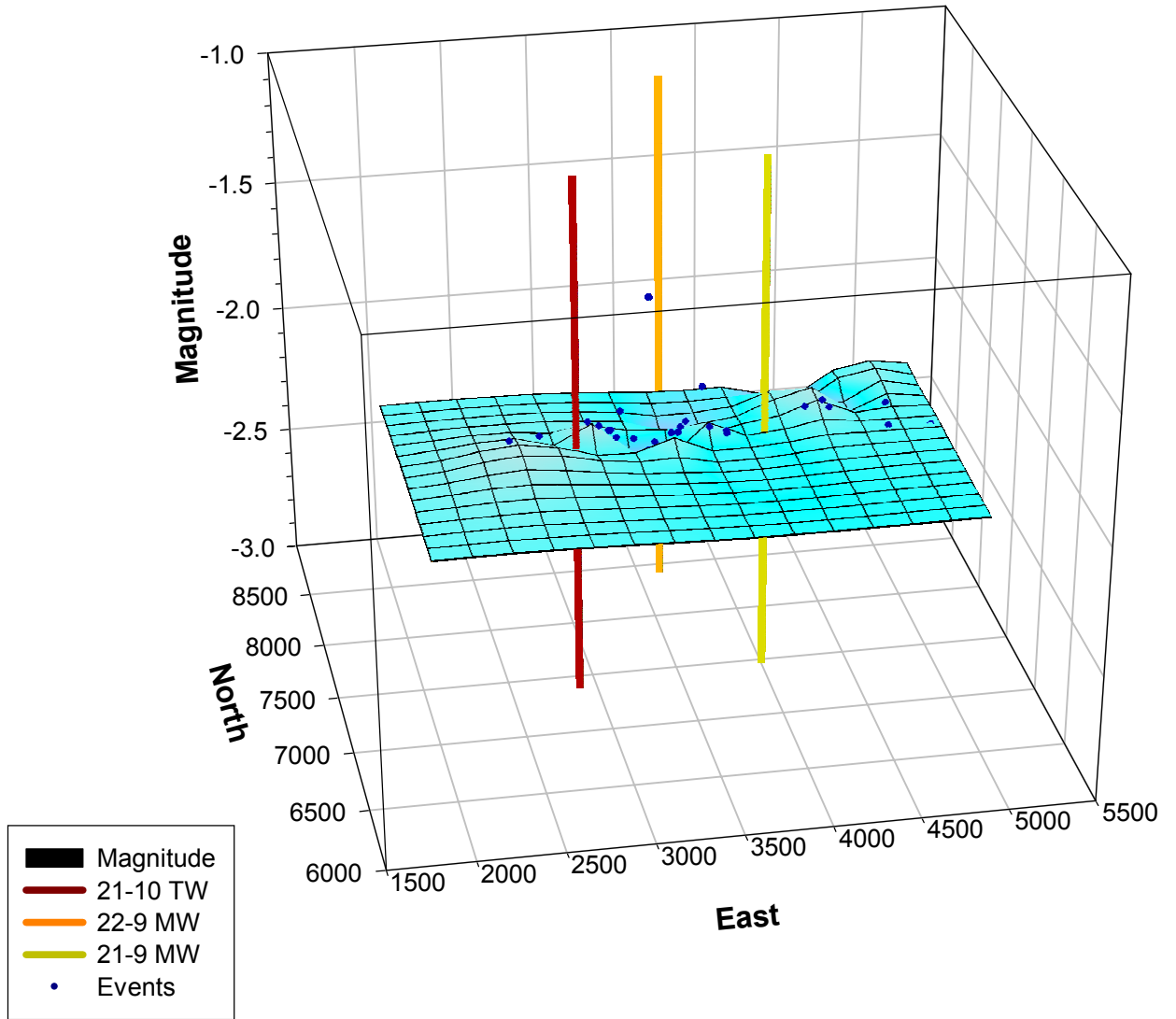


Figure 23. Contoured distribution of event magnitudes for those recorded during the 0512 treatment along with their individual magnitude values. The treatment well is 21-10 and sensors employed in the magnitude calculation are as shown in Figure 2. In this and all subsequent figures, the source parameters are shown in plan view.

Phase 1, 0514 Hydraulic Fracture

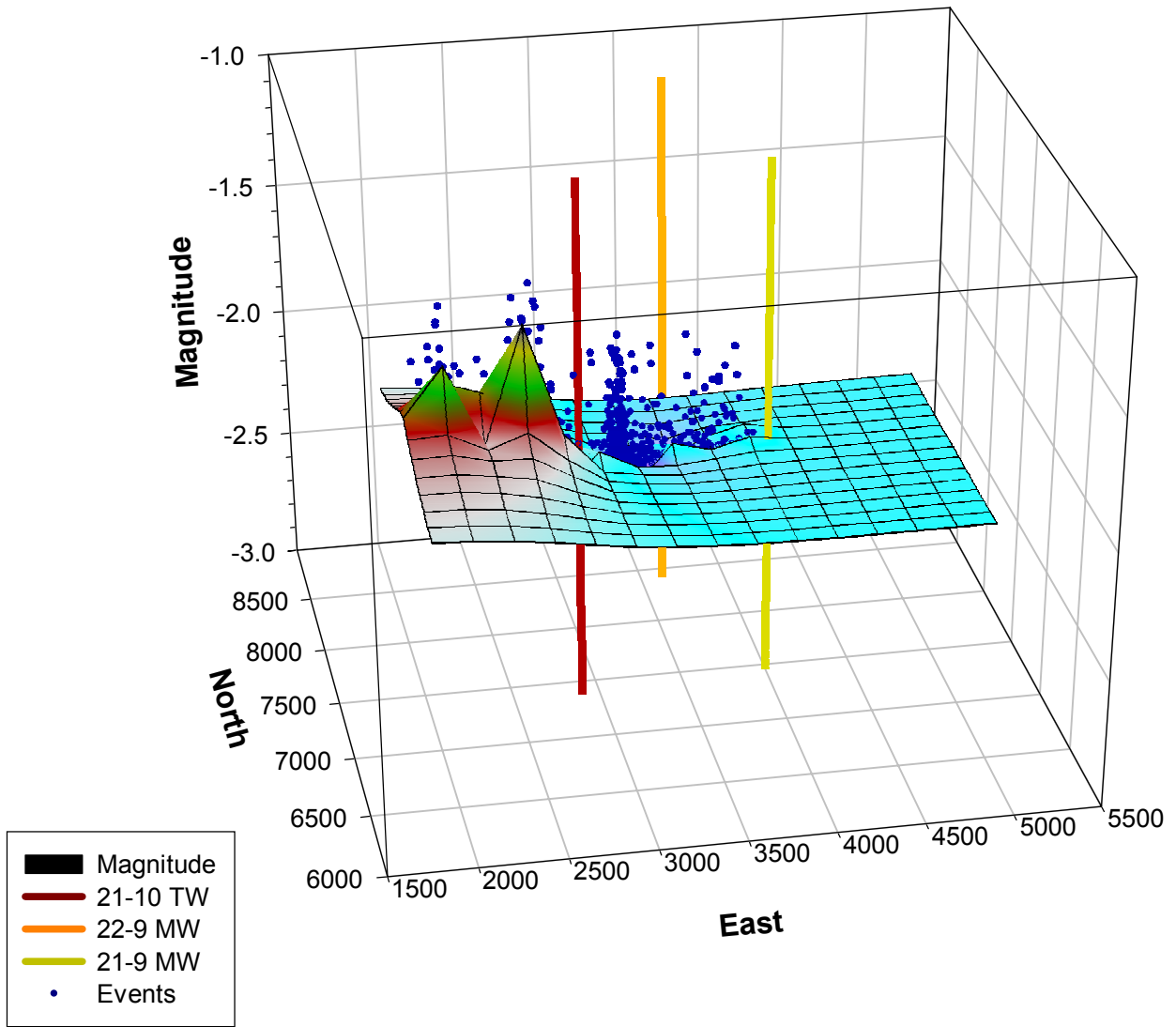


Figure 24.. Contoured distribution of event magnitudes for those recorded during the 0514 treatment along with their individual magnitude values. The treatment well is 21-10 and sensors employed in the magnitude calculation are as shown in Figure 3.

Phase 1, 0516 Hydraulic Fracture

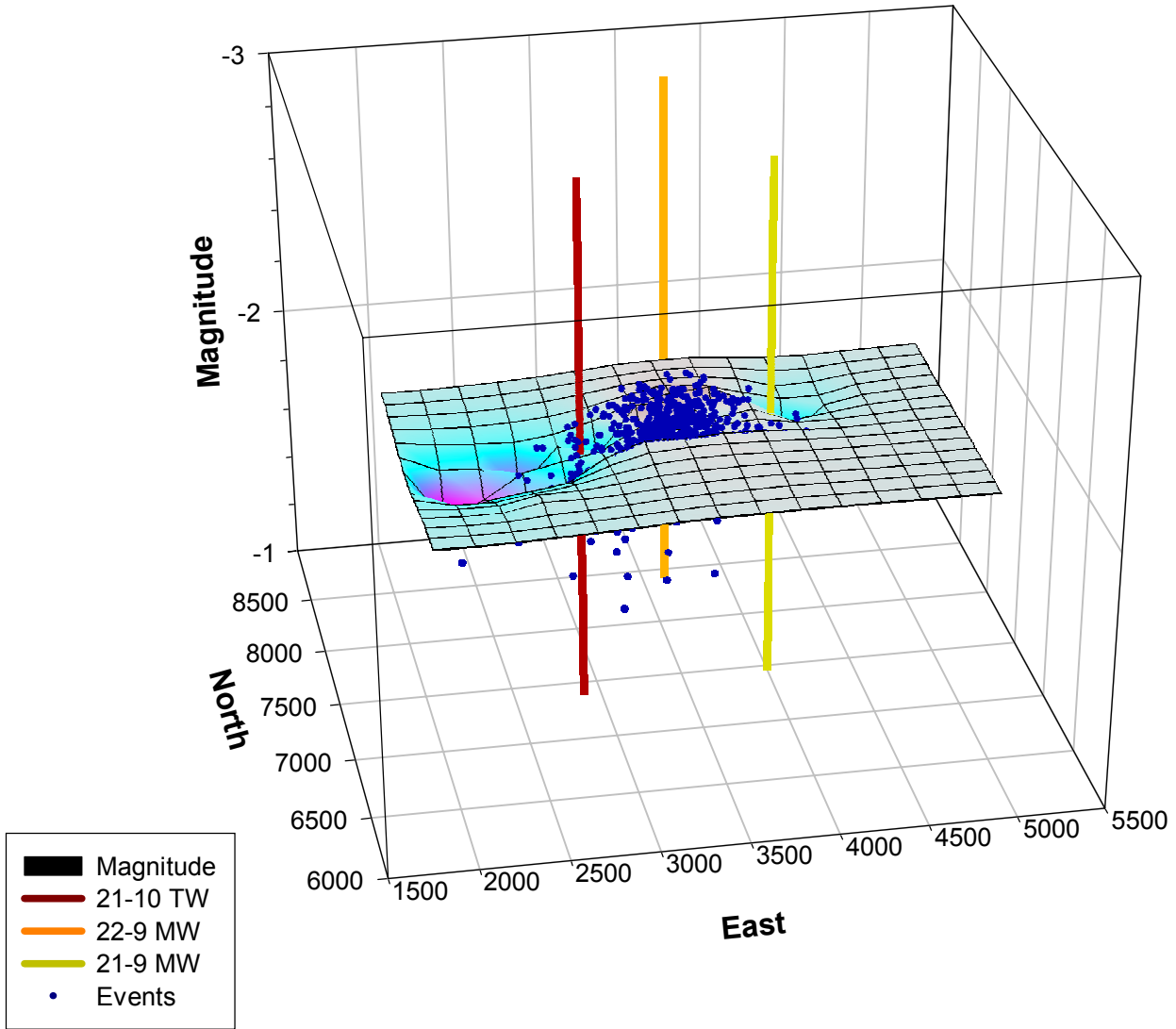


Figure 25. Contoured distribution of event magnitudes for those recorded during the 0516 treatment along with their individual magnitude values. The treatment well is 21-10 and sensors employed in the magnitude calculation are as shown in Figure 4.

Phase 1, 0512 Hydraulic Fracture

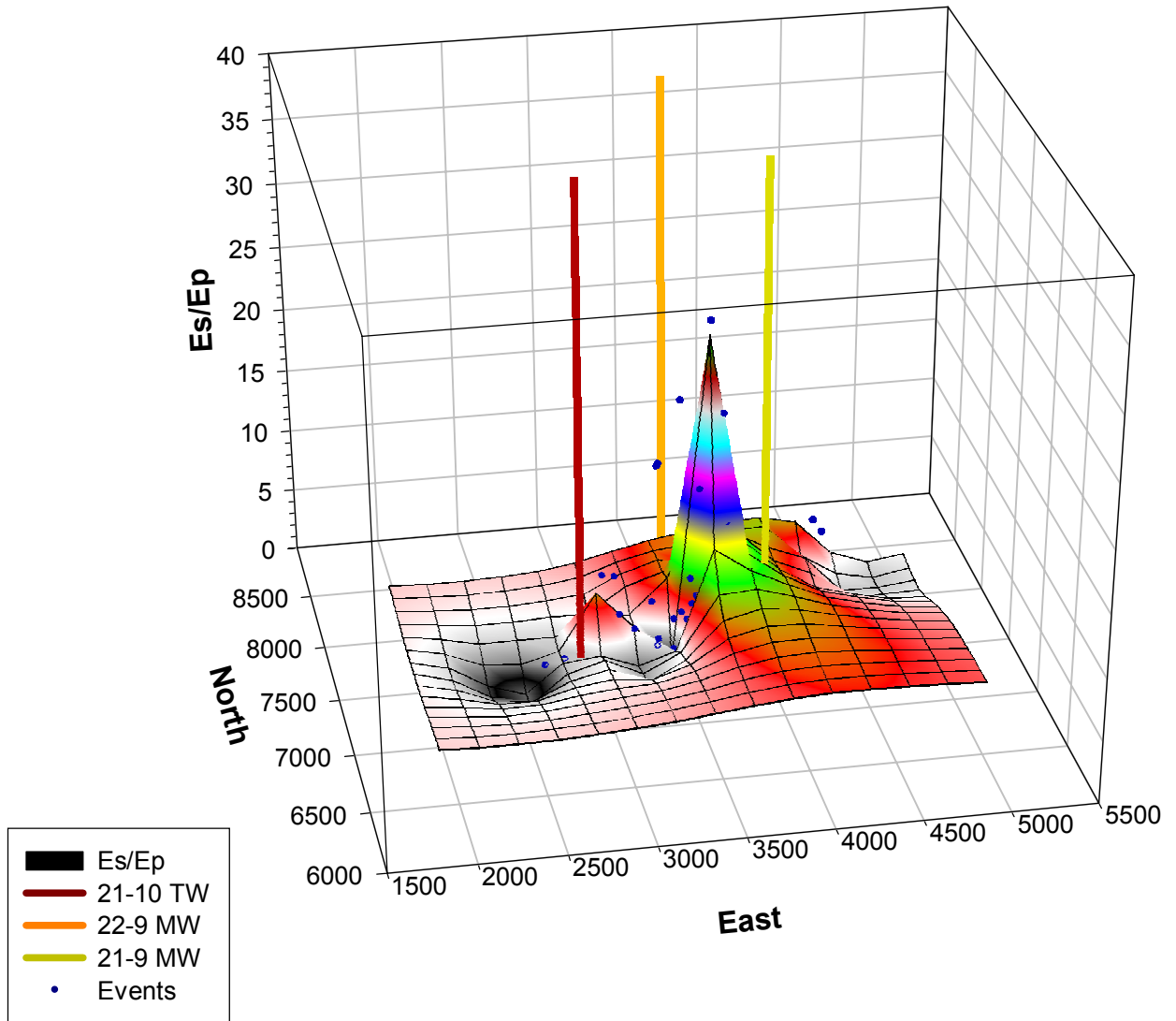


Figure 26. Contoured distribution of E_s/E_p values for those events recorded during the 0512 treatment along with their individual values. The treatment well is 21-10 and sensors employed in the calculations are as shown in Figure 2.

Phase 1, 0514 Hydraulic Fracture

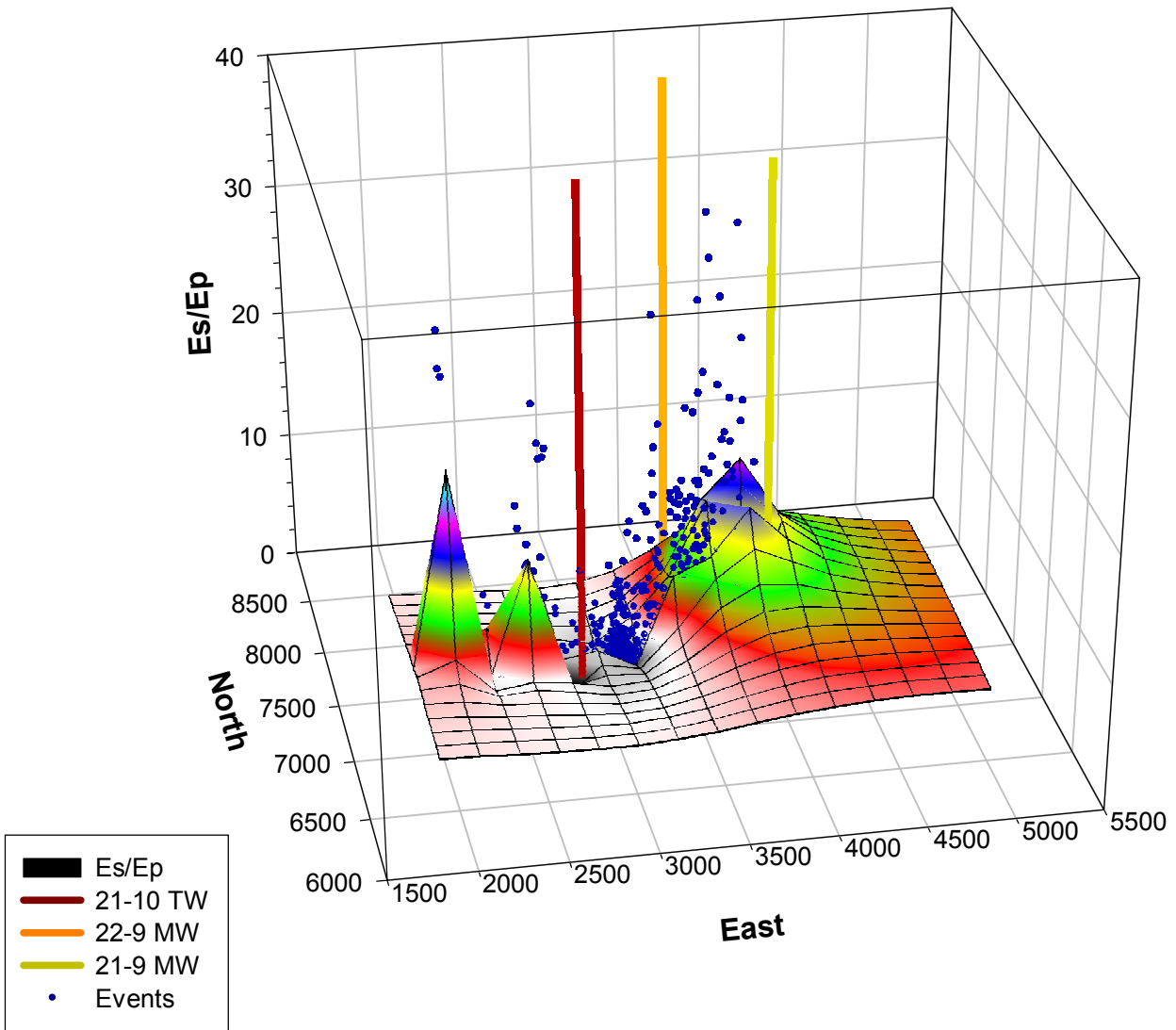


Figure 27. Contoured distribution of Es/Ep values for those events recorded during the 0514 treatment along with their individual values. The treatment well is 21-10 and sensors employed in the Es/Ep calculation are as shown in Figure 3.

Phase 1, 0516 Hydraulic Fracture

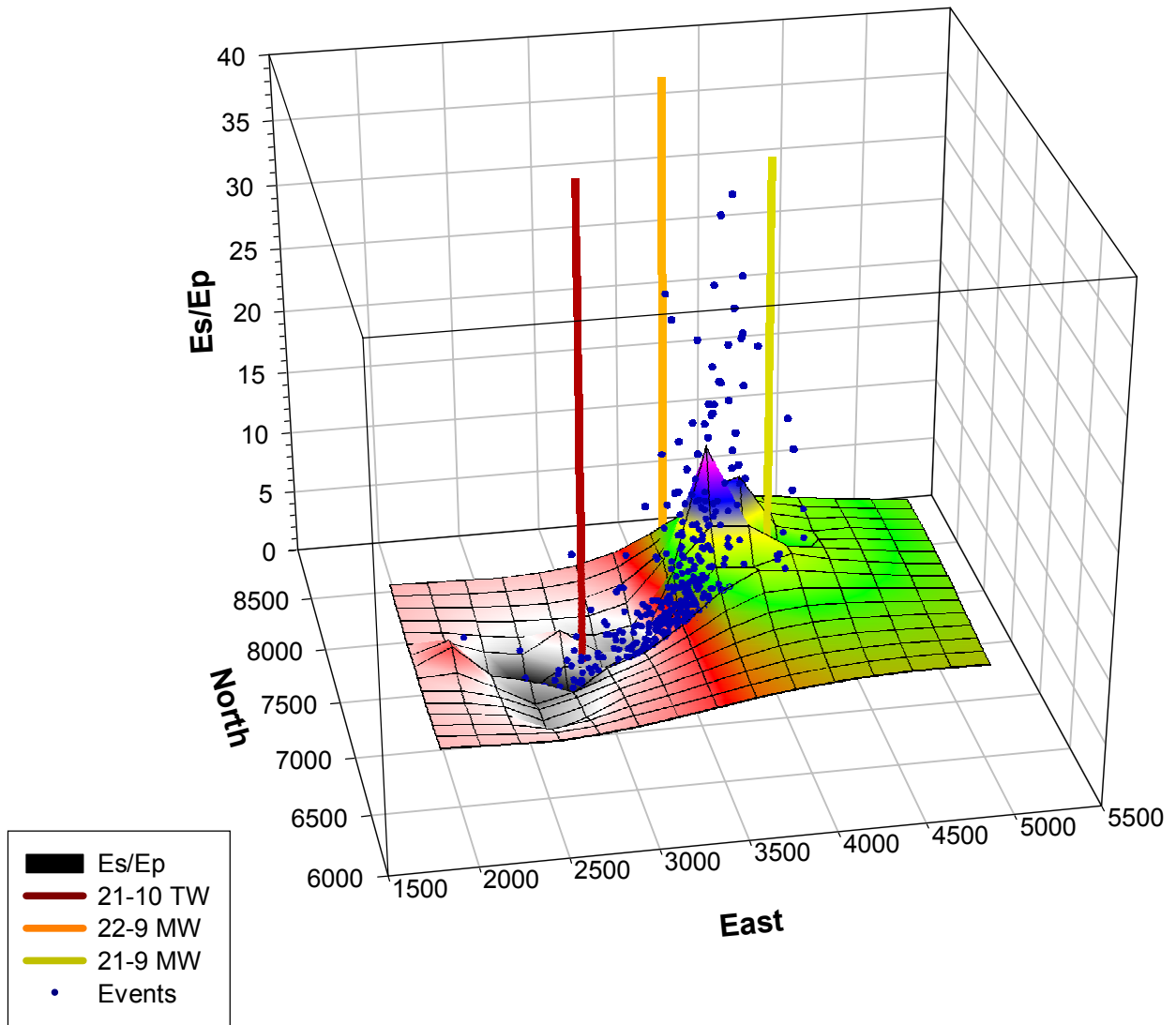


Figure 28. Contoured distribution of E_s/E_p values for those events recorded during the 0516 treatment along with their individual values. The treatment well is 21-10 and sensors employed in the calculations are as shown in Figure 4.

Phase 1, 0514 Hydraulic Fracture

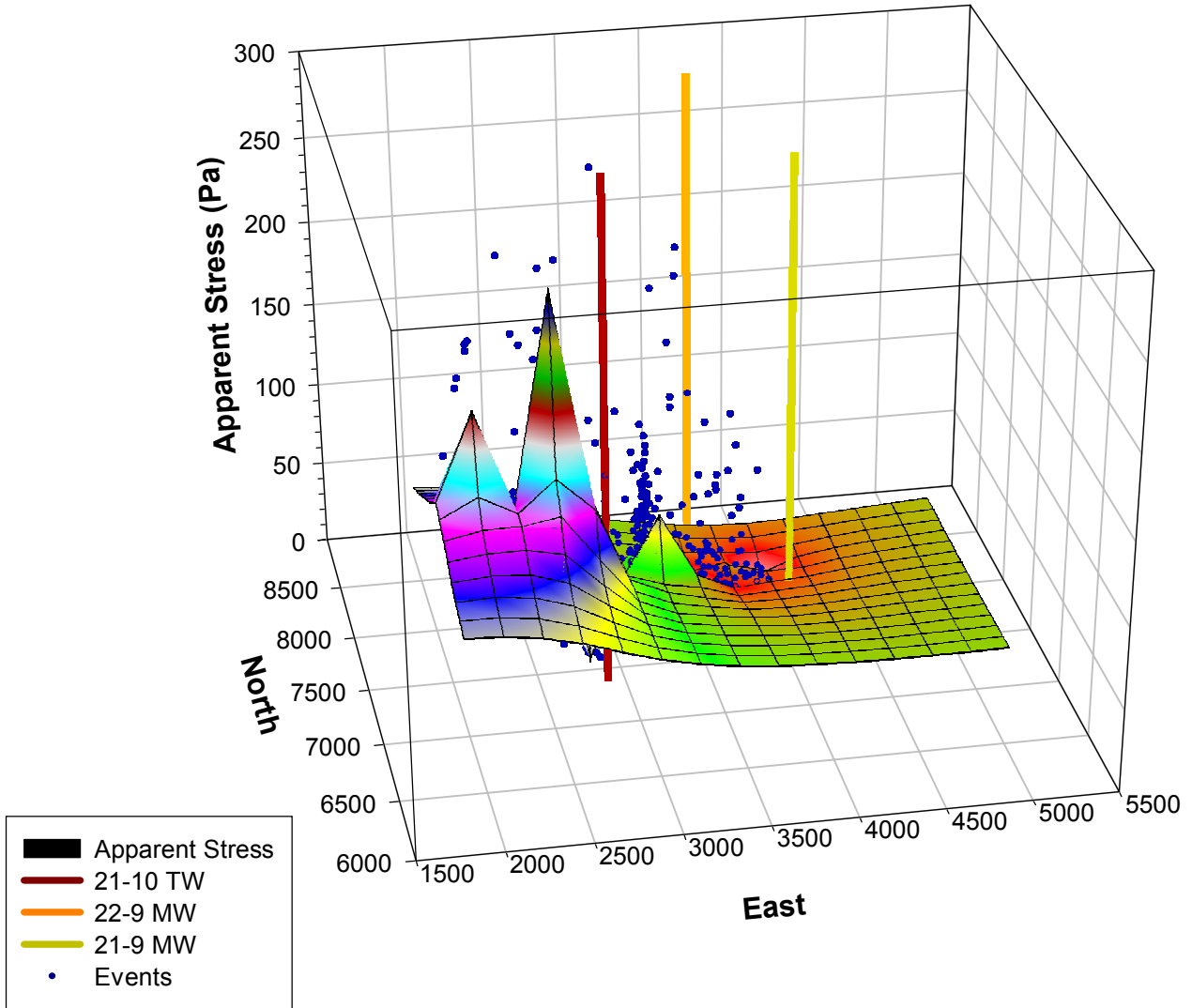


Figure 29. Contoured distribution of apparent stress values for those events recorded during the 0514 treatment along with their individual values. The treatment well is 21-10 and sensors employed in the apparent stress calculation are as shown in Figure 3.

Phase 1, 0714 Hydraulic Fracture

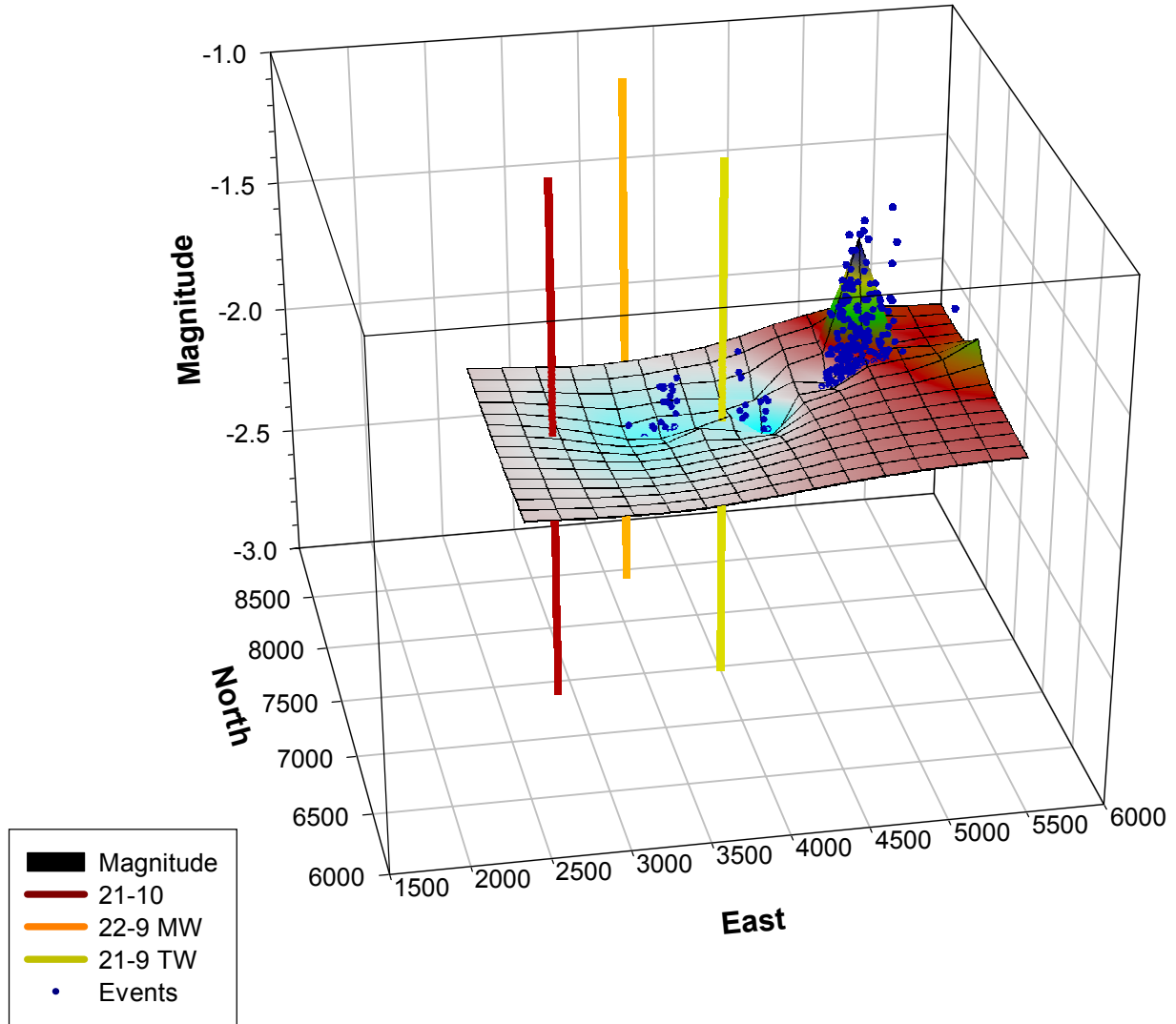


Figure 30. Contoured distribution of event magnitude values for those events recorded during the 0714 treatment along with their individual values. The treatment well is 21-9 and sensors employed in the magnitude calculation are as shown in Figure 16.

Phase 1, 0716 Hydraulic Fracture

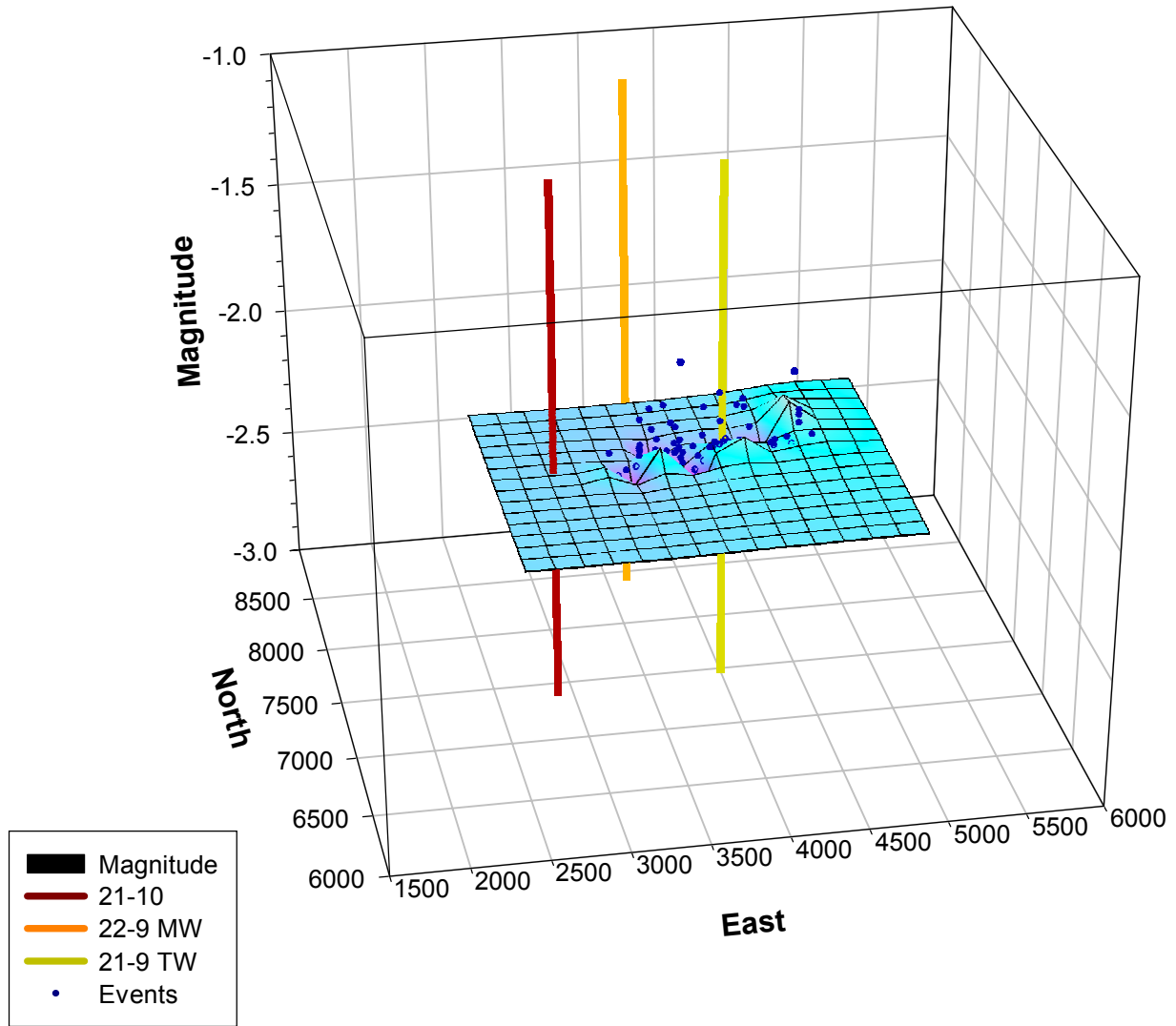


Figure 31. Contoured distribution of event magnitude values for those events recorded during the 0716 treatment along with their individual values. The treatment well is 21-9 and sensors employed in the magnitude calculation are as shown in Figure 16.

Phase 1, 0718 Hydraulic Fracture

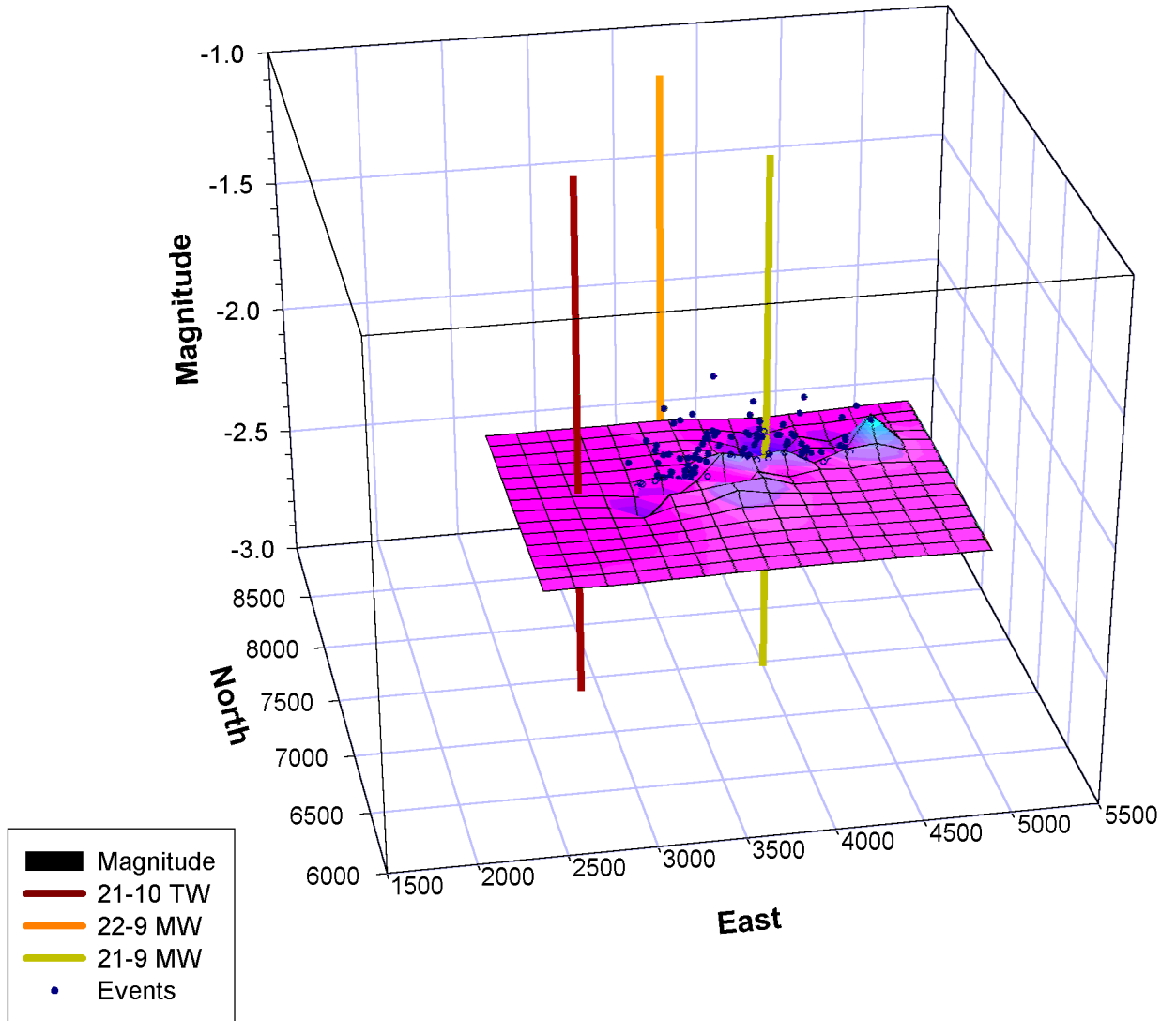


Figure 32. Contoured distribution of event magnitude values for those events recorded during the 0718 treatment along with their individual values. The treatment well is 21-9 and sensors employed in the magnitude calculation are as shown in Figure 16.

Phase 1, 0714 Hydraulic Fracture

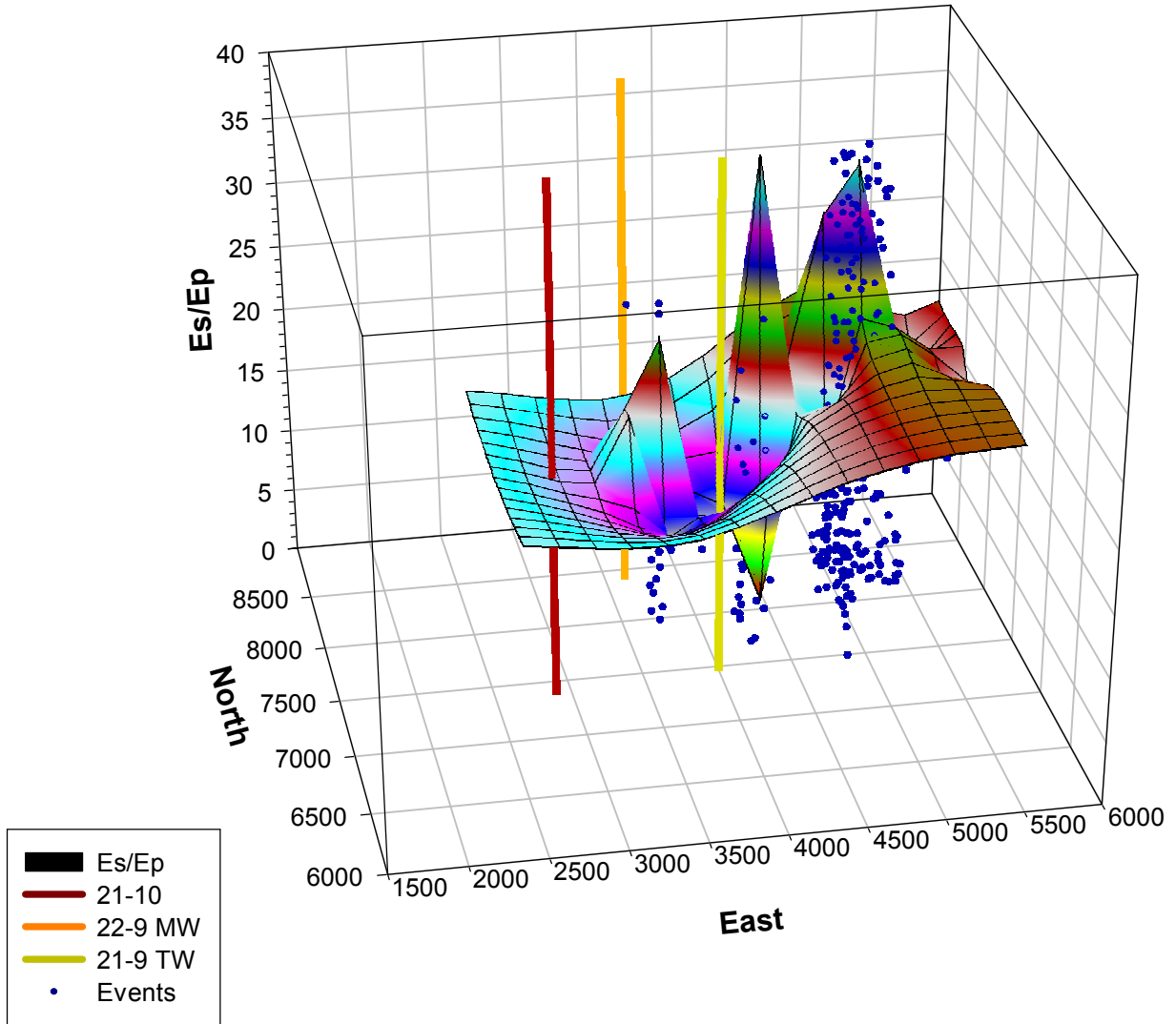


Figure 33. Contoured distribution of E_s/E_p values for those events recorded during the 0714 treatment along with their individual values. The treatment well is 22-9 and sensors employed in the E_s/E_p calculation are as shown in Figure 16.

Phase 1, 0714 Hydraulic Fracture

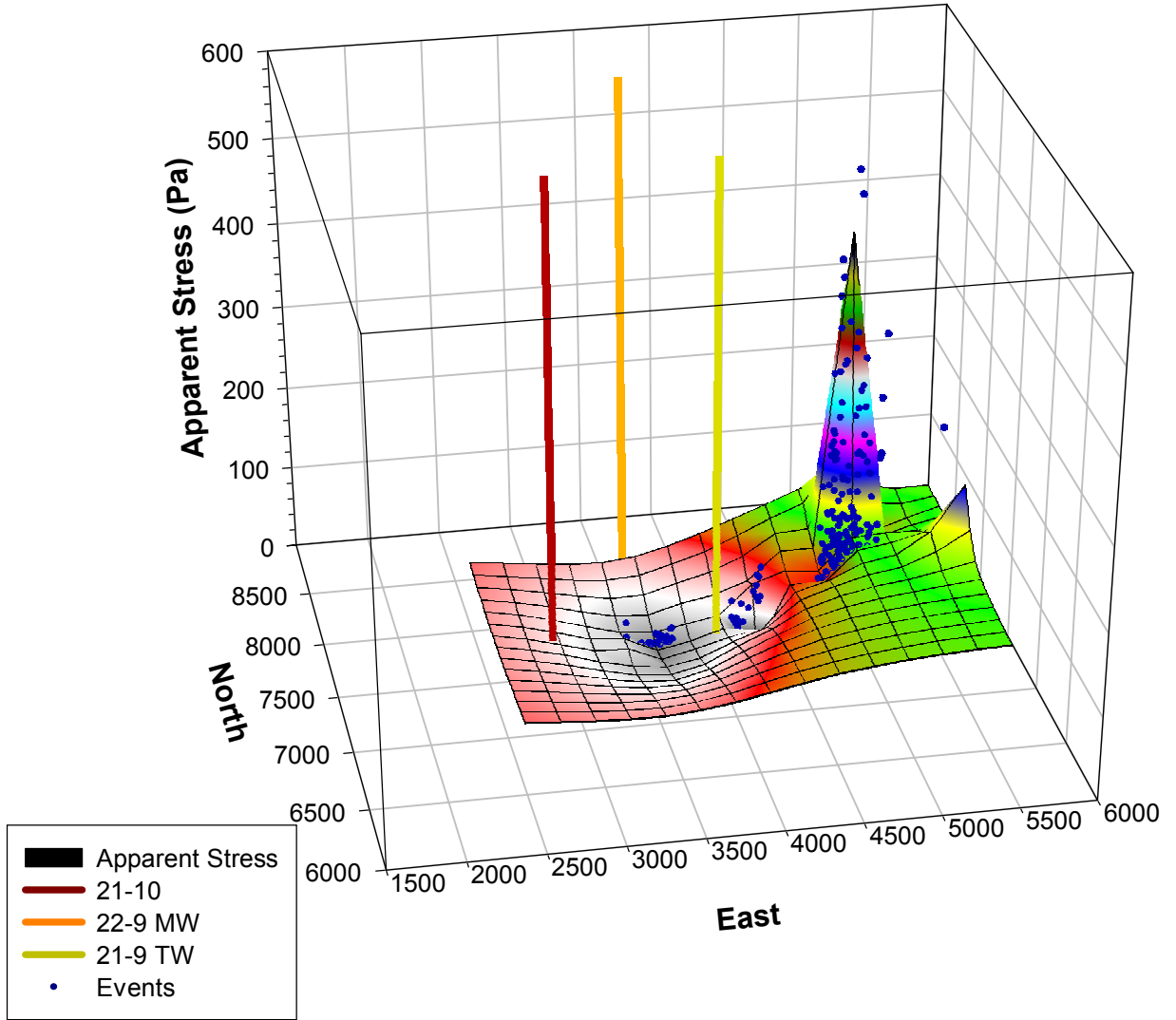


Figure 34. Contoured distribution of apparent stress values for those events recorded during the 0714 treatment along with their individual values. The treatment well is 22-9 and sensors employed in the calculations are as shown in Figure 16.

Phase 1, 0716 Hydraulic Fracture

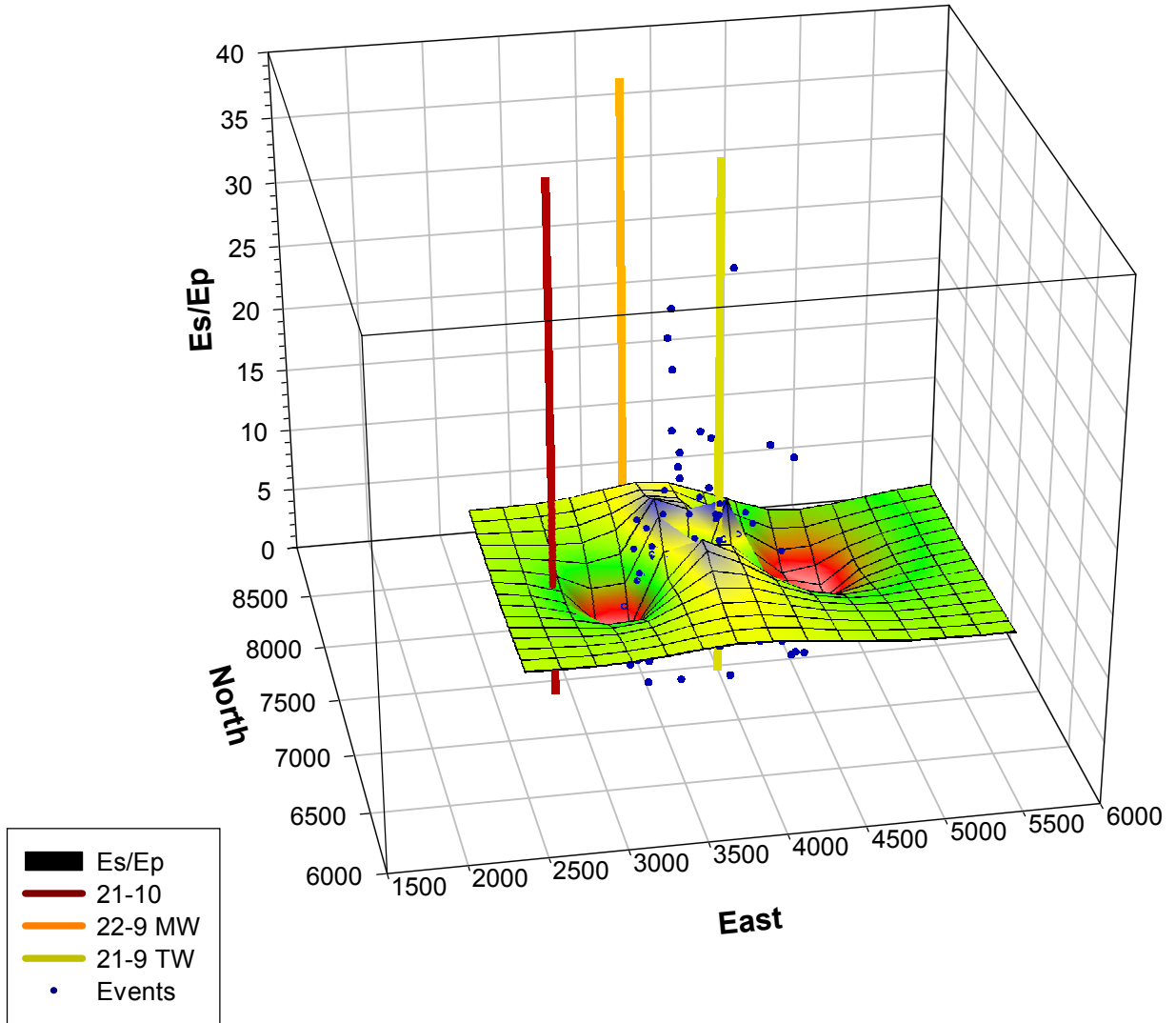


Figure 35. Contoured distribution of Es/Ep values for those events recorded during the 0716 treatment along with their individual values. The treatment well is 22-9 and sensors employed in the Es/Ep calculation are as shown in Figure 16.

Phase 1, 0718 Hydraulic Fracture

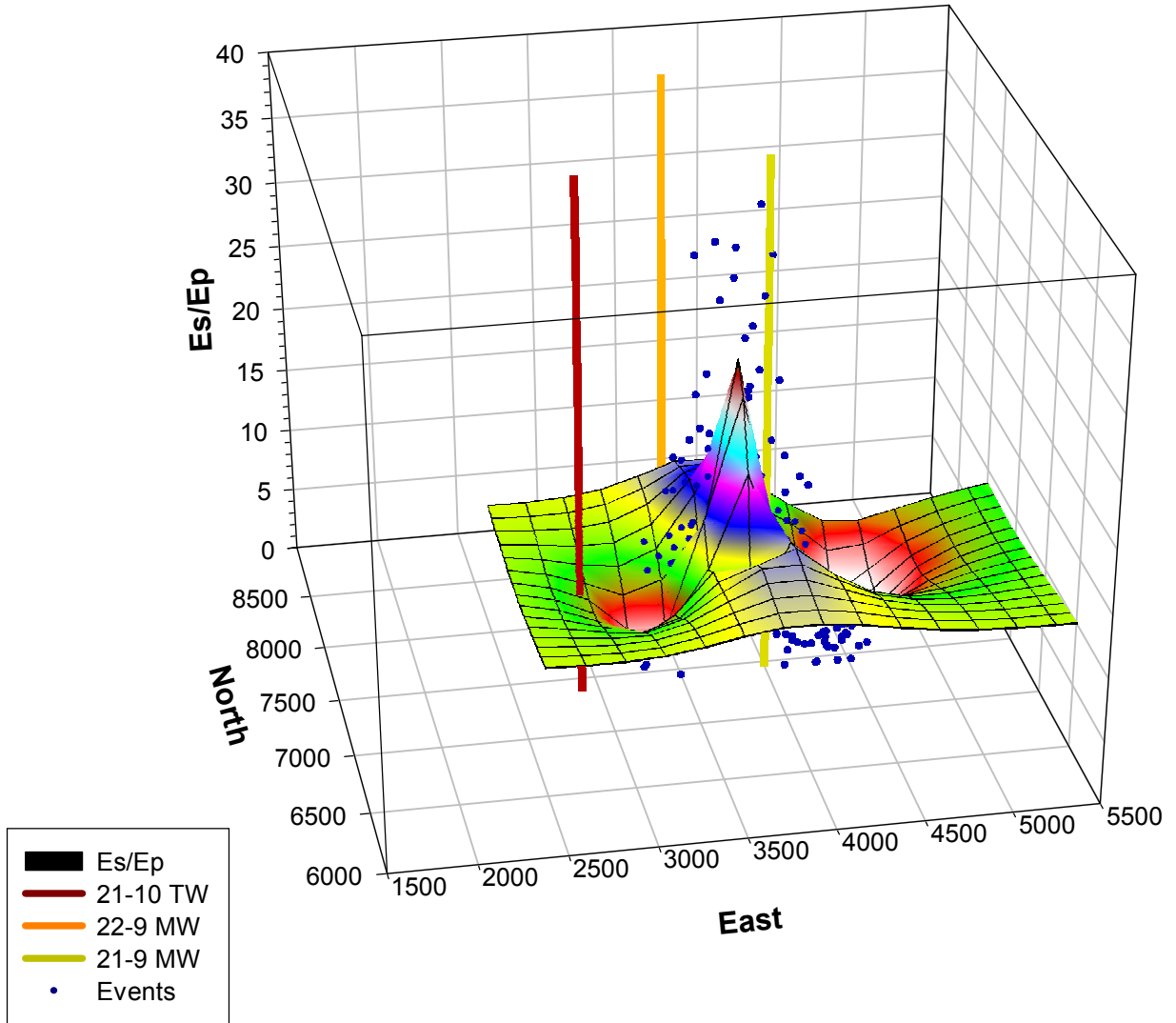


Figure 36. Contoured distribution of Es/Ep values for those events recorded during the 0718 treatment along with their individual values. The treatment well is 22-9 and sensors employed in the Es/Ep calculation are as shown in Figure 16.

Phase 1, 0718 Hydraulic Fracture

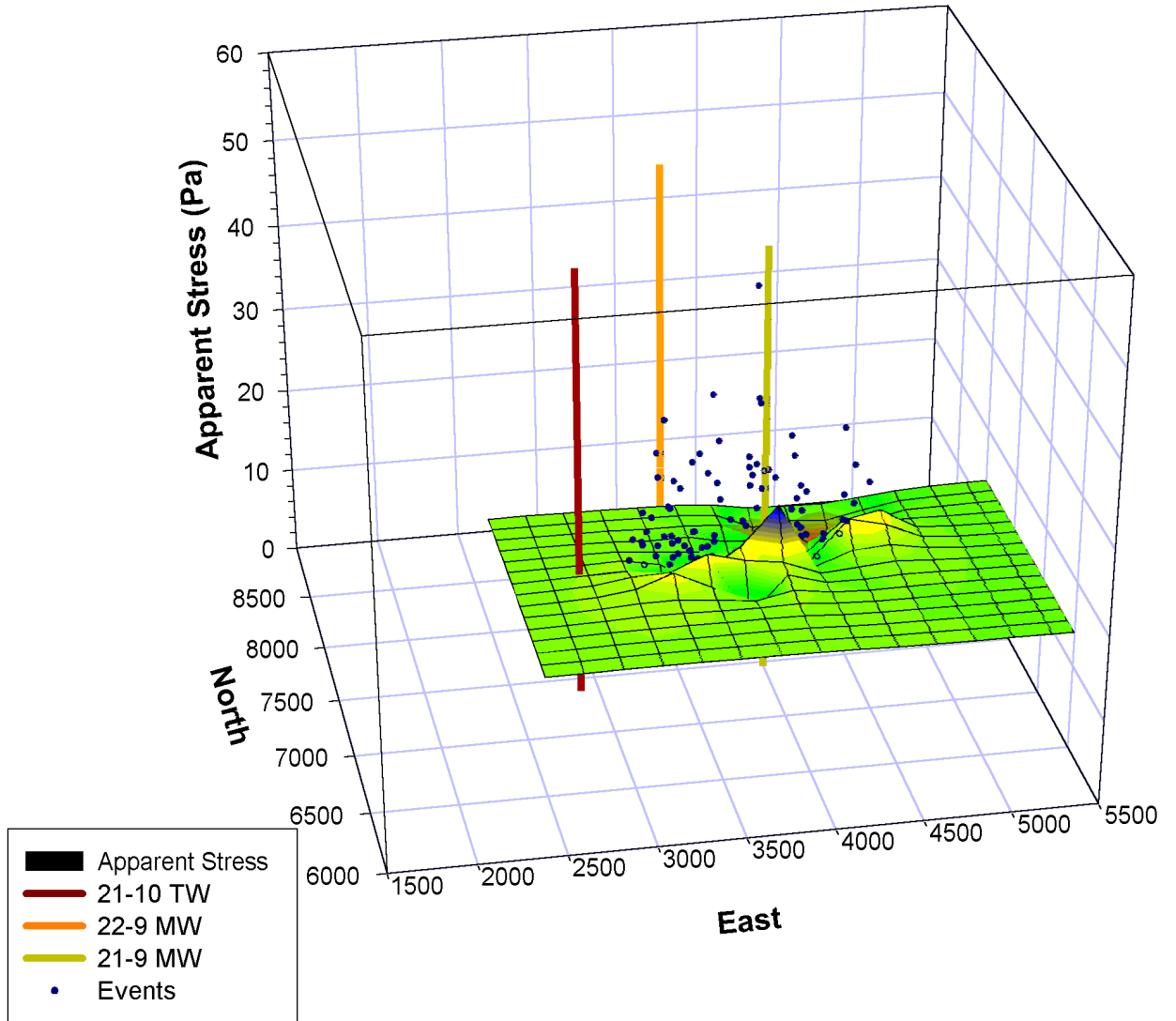


Figure 37. Contoured distribution of apparent stress values for those events recorded during the 0718 treatment along with their individual values. The treatment well is 22-9 and sensors employed in the calculations are as shown in Figure 16.